U.S. DEPARTMENT OF ENERGY

Ultrasonic Characterization of Cast Austenitic Stainless Steel Microstructure: Discrimination between Equiaxed- and Columnar-Grain Material – An Interim Study

P Ramuhalli   BE Watson
MS Good   TJ Peters
AA Diaz   M Dixit
MT Anderson   LJ Bond

October 2009

Pacific Northwest
NATIONAL LABORATORY

Proudly Operated by **Battelle** *Since 1965*

DISCLAIMER

This report was prepared as an account of work sponsored by an agency of the United States Government. Neither the United States Government nor any agency thereof, nor Battelle Memorial Institute, nor any of their employees, makes **any warranty, express or implied, or assumes any legal liability or responsibility for the accuracy, completeness, or usefulness of any information, apparatus, product, or process disclosed, or represents that its use would not infringe privately owned rights**. Reference herein to any specific commercial product, process, or service by trade name, trademark, manufacturer, or otherwise does not necessarily constitute or imply its endorsement, recommendation, or favoring by the United States Government or any agency thereof, or Battelle Memorial Institute. The views and opinions of authors expressed herein do not necessarily state or reflect those of the United States Government or any agency thereof.

Ultrasonic Characterization of Cast Austenitic Stainless Steel Microstructure: Discrimination between Equiaxed- and Columnar-Grain Material – An Interim Study

P Ramuhalli
MS Good
AA Diaz
MT Anderson

BE Watson
TJ Peters
M Dixit
LJ Bond

October 2009

Pacific Northwest National Laboratory
Richland, Washington 99352

Executive Summary

Ultrasonic nondestructive evaluation (NDE) and inspection of cast austenitic stainless steel (CASS) components used in the nuclear power industry is neither as effective nor reliable as is needed. With current ultrasonic methods these limitations are in large part due to the detrimental effects of wave-microstructure interactions on the interrogating ultrasonic beam and interference that results from ultrasonic backscatter. The root cause of these phenomena is the coarse-grain microstructure inherent to this class of materials. Some ultrasonic techniques are found to perform better for particular microstructural classifications and this has led to the hypothesis that an ultrasonic inspection can potentially be optimized for a particular microstructural class. For optimized ultrasonic technique selection, methods will be needed to reliably classify the microstructure in-situ, which is then used to guide the selection and optimization of the inspection. This document summarizes scoping experiments that investigate potential in-situ ultrasonic methods for classification and/or characterization of the material microstructures in CASS components, when making measurements from the outside surface of a pipe.

The focus of this preliminary study was to evaluate ultrasonic measurement methods to determine if responses from different known microstructures can be differentiated and hence if in-service characterization of cast austenitic stainless steel (CASS) is potentially feasible. On the basis of an initial literature evaluation, two ultrasonic parameters, (i) the time-of-flight ratio between shear and longitudinal waves and (ii) the attenuation for normal incidence longitudinal waves, were selected for investigation. Scoping experiments were performed to determine the ability of these measured parameters to discriminate between different microstructures in CASS components. The objective was to determine if a more thorough and staged exploration would be justified in progressing toward the real-time characterization of CASS for use as feedback to optimize current or new ultrasonic in-service inspection methodologies. With this objective in mind, measurements were restricted to techniques that potentially should be robust if carried forward to an eventual field implementation.

The first parameter investigated was a time-of-flight ratio of a normal incidence shear wave to that of a normal incidence longitudinal wave (TOFRSL). The ratio removes dependency on component thickness which may not be accurately known or reported in the field. The second parameter was the attenuation of a normal incidence longitudinal wave. The selected CASS specimens used for the experimental study were five equiaxed-grain material samples and five columnar-grain material samples, and these were used for a two-class discrimination problem.

TOFRSL estimates and a threshold algorithm classified all 10 material samples correctly and indicated a potentially reliable and robust technique. Qualitative longitudinal wave attenuation estimates and a threshold algorithm also classified all 10 materials samples correctly; however, the technique was, at least in this initial study, not as robust as TOFRSL. The experiments provided promising results and demonstrated that there is a good basis to believe that potential exists for further development of these techniques for real-time classification of CASS material. However, the initial measurements reported here need to be confirmed with measurements on additional specimens that represent a wider range of classes of microstructures.

In developing this investigation into the potential for "ultrasonic microstructure classification techniques using in-situ measurements on CASS," work will focus on refining TOFRSL and acoustic

attenuation measurement protocols, conducting proof-of-concept experiments for acoustic backscatter as a function of incident angle, and other techniques that can be used to characterize inhomogeneous and anisotropic material. An important aspect of backscatter is the ability to provide feature depth resolution (through the use of appropriate time-gates) while the two estimated parameters of TOFRSL and attenuation are by their nature averaged over the pipe wall thickness. Continuing experimental work includes:

- Verifying repeatability of the initial experiments, and confirming the results using additional specimens that are representative of the columnar and equiaxed grain structure (as well as mixed grain structures). The microstructures selected should seek to be representative of the majority of microstructures that can be encountered in current legacy U.S. nuclear power plant components.

- Enhancing TOFRSL estimates by investigating more effective coupling, including potential use of electromagnetic acoustic transducers (EMATs) to transmit and receive normal incidence shear waves, and moving toward a quantitative estimate by use of arrival time calibration and compensation for diffraction.

- Enhancing acoustic attenuation estimates by investigating more effective coupling, including use of electromagnetic acoustic transducers (EMATs), shear-wave attenuation measurements, and computing the estimates over a broader frequency range through the use of broadband transducers employing swept frequency excitation.

- Conducting backscatter measurements for improved depth resolution in classifying CASS microstructure, with known through wall variability.

- Evaluating other ultrasonic or electromagnetic methods used for microstructure and material characterization, used in other applications, that can be leveraged and applied to the CASS microstructural characterization challenge.

- Assessing the applicability of these techniques to characterizing cast primary circuit components (safe ends, elbows, or pipes) through inspection from the ID surface.

Acronyms and Abbreviations

BNC	bayonet Neill-Concelman
CASS	cast austenitic stainless steel
CCASS	centrifugally cast austenitic stainless steel
CCD	charge-coupled device
IPF	inverse pole figure
EBSD	electron backscatter diffraction
EMAT	electromagnetic acoustic transducer
EPRI	Electric Power Research Institute
FFT	fast Fourier transform
HOS	higher order statistics
ID	inner diameter
JEOL	Japan Electron Optics Laboratory Company, Inc.
MED	minimum entropy deconvolution
NDE	nondestructive examination or evaluation
OD	outer diameter
PISC	Programme for the Inspection of Steel Components
PNNL	Pacific Northwest National Laboratory
RF	radio frequency
RMS	root mean square
SAFT	synthetic aperture focusing technique
SCASS	statically cast austenitic stainless steel
SNR	signal-to-noise ratio
SEM	scanning electron microscopy
SH	Pure shear or shear wave with horizontal polarization
SV	shear wave with vertical polarization
TOF	time of flight
TOFRSL	time-of-flight ratio of a normal incidence shear wave to a normal incidence longitudinal wave

Contents

Figures

Tables

1.0   Introduction

Ultrasonic nondestructive evaluation (NDE) and inspection of cast austenitic stainless steel (CASS) components used in the nuclear power industry is neither as effective nor as reliable as is needed. With current ultrasonic methods, these limitations are in large part due to detrimental effects of wave-microstructure interactions on the interrogating ultrasonic beam and interference that results from ultrasonic backscatter (Diaz et al. 1998; EPRI 2005). The root cause of these phenomena is the coarse-grain microstructure inherent to this class of materials (Jeong 1987; Kupperman et al. 1987). Pump bowls and elbow piping components consist of statically cast austenitic stainless steel (SCASS), which has very large grains. Many pressurized water reactors use centrifugally CASS (CCASS) piping to inter-connect major components of the reactor system. CCASS is a coarse-grained material that has a variety of microstructures which are dependent on the fabrication process (Northcott and Dickin 1944; Northcott and McLean 1945; Cumberland 1963; Jeong 1987). The engineering properties of this material made it a material of choice for selected designs of nuclear power reactor systems. However, the fabrication processes result in a variety of microstructures that are difficult to inspect ultrasonically. Increased scattering from the coarse-grain microstructure results in higher noise levels and increased attenuation, both of which adversely impact flaw detection capabilities (EPRI 2005). The use of lower ultrasonic frequencies decreases interference from ultrasonic backscatter and increases penetration (EPRI 2005). However, this is at the expense of decreased spatial resolution. Some ultrasonic techniques are found to perform better for particular microstructural classifications (Hudgell and Gray 1985) and this has led to the hypothesis that an ultrasonic inspection can potentially be optimized for a particular microstructural class. −For optimal ultrasonic technique selection, methods will be needed to reliably classify the microstructure in-situ, which is then used to guide the selection and optimization of the inspection[a] (Jeong 1987; Kupperman et al. 1987; Jeong and Ammirato 1989). Examples of such optimization include the ability to modify sensor signal processing algorithms to enhance synthetic aperture focusing technique (SAFT) images (Silverstein and Thomas 1993), optimize SAFT probes to improve the signal-to-noise ratio (SNR) (Nageswaran and Whittle 2008), and apply simulation models to better understand ultrasonic wave propagation in polycrystalline materials (Jenson et al. 2009).

This report documents scoping experiments that investigate potential in-situ ultrasonic methods for classification and/or characterization of material microstructures in CASS components, when making measurements from the outside surface of the pipe or component. The focus of this study was to evaluate ultrasonic measurement methods to determine if responses from different known microstructures can be differentiated, and hence if in-service characterization of cast austenitic stainless steel (CASS) is potentially feasible. Because the focus was on eventual in-service characterization, measurements were restricted to techniques that potentially should be robust if carried forward to an eventual field implementation. With this objective in mind, available literature was evaluated to determine the range of interactions between coarse-grained material on ultrasonic waves, and their impact on nondestructive evaluation. On the basis of this initial literature evaluation, two ultrasonic parameters were selected for initial investigation. The first parameter investigated in this study was the time-of-flight ratio of a normal incidence shear wave to that of a normal incidence longitudinal wave (TOFRSL). The ratio removes dependency on component thickness which may not be accurately known or reported in the field. The second parameter investigated was attenuation of a normal incidence longitudinal wave. Scoping

---

(a) Hildebrand BP, MS Good, and AA Diaz. 1991. *Ultrasonic Classification of Centrifugally Cast Stainless Steel Utilizing the Rayleigh Critical Angle Technique.* Technical Letter Report from PNNL to the NRC.

experiments were performed to determine the ability of these measured parameters to discriminate between different microstructures in CASS components. The objective was to determine if a more thorough and staged exploration would be justified in progressing toward the real-time characterization of CASS for use as feedback to optimize current or new ultrasonic in-service inspection methodologies. The results of this preliminary study are presented in this report.

This rest of this report is organized as follows. Section 2 provides a brief discussion of CASS, material-ultrasonic interactions common to CASS that create a challenge for ultrasonic inspection, and signal processing tools for enhancing ultrasonic measurements from CASS. The latter is included with the premise that signal processing techniques may provide useful insight for material characterization. Section 3 describes experiments to evaluate two qualitative ultrasonic parameters as a means of discriminating between two extreme and very different CASS materials - equiaxed-grain material and columnar-grain material. The ultrasonic parameters selected for this study are TOFRSL, and attenuation in a normal incidence longitudinal wave. Details of the specimens, experiments and data analysis, along with a discussion of the results, are provided in this section. Section 4 summarizes the results and provides recommendations for further investigation. Appendix A presents characterization results of one of the specimens using scanning electron microscopy (SEM) and electron backscatter diffraction (EBSD) analysis. An introductory overview of EBSD for material characterization is provided in Appendix B. Finally, Appendix C has the details of the calculations that were used for estimating longitudinal wave attenuation.

2.0 Cast Austenitic Stainless Steel

Cast austenitic stainless steel (CASS) commonly used in nuclear power plants is a polycrystalline coarse-grained material that is elastically anisotropic. The interaction of ultrasonic waves with such material results in phenomena such as sound speed variations, ultrasonic beam deviation, high attenuation and high background acoustic noise caused by scattering, and phase variations across a wave front. These phenomena make reliable ultrasonic inspections extremely challenging but can potentially form the basis for methods of classifying and characterizing CASS microstructures based on ultrasonic measurements. However, high levels of background noise can impact the measurements, resulting in poor discrimination capability. To overcome the effects of noise and improve the signal-to-noise ratio (SNR), various signal processing techniques may be necessary. This section provides a brief review of CASS material microstructures, followed by a discussion of material-ultrasonic interactions common to CASS. This is followed by a brief review of signal processing techniques potentially applicable to ultrasonic signals from CASS materials.

2.1 CASS Material

The grain size of wrought stainless steel is small in contrast to CASS because of extensive material reduction and refining. Each cubic austenitic grain preserves its anisotropic properties, but grains are small relative to the ultrasonic wavelength used by typical inspection processes. Acoustic backscatter causes signal amplitude loss as the wave propagates across numerous grain boundaries where a change in acoustic impedance (product of material density and sound speed) exists. Grains are generally randomly oriented relative to one another; thus, wrought stainless steel acoustically behaves as a quasi-isotropic material for ultrasonic waves typically used during in-service inspection.

CASS components, unlike wrought austenitic stainless steel, are typically cast to a near net shape of the final component dimensions. Statically CASS (SCASS) components are typically large and the sand-cast mold insulates the solidified metal. A coarse-grain material results from the slower cooling rate and the microstructure not being refined. A rotating casting mold is used during centrifugally CASS (CCASS) piping fabrication. Microstructure and macrostructure are affected by material chemistry, mold and metal temperatures, metal pour rate, cast rotation rate, and mold vibration (Northcott and Dickin 1944; Northcott and McLean 1945; Cumberland 1963). Macrostructure includes the homogeneity of the microstructure, texture for direction-dependent features, and residual stresses (Goebbels 1994). Similar comments may be made for other austenitic stainless steel portions of the reactor system that employ cast-like fabrication methods. This includes regions such as welds, weld overlay repair of welds, and differential welds where a weld bead is applied and dendrites form during solidification. Grain orientation within the weld bead is a function of nucleation sites and heat flow. Successive weld beads are applied as the material is built up and a well established columnar dendritic pattern is typical. CASS can be columnar dendritic; however, a variety of other microstructures such as planar, cellular, cellular dendritic, and equiaxed dendritic may exist (Jeong 1987).

Columnar grain and equiaxed-grain materials are evident from macrographs of CCASS specimens as shown in Figure 2.1, Figure 2.2, and Figure 2.3.
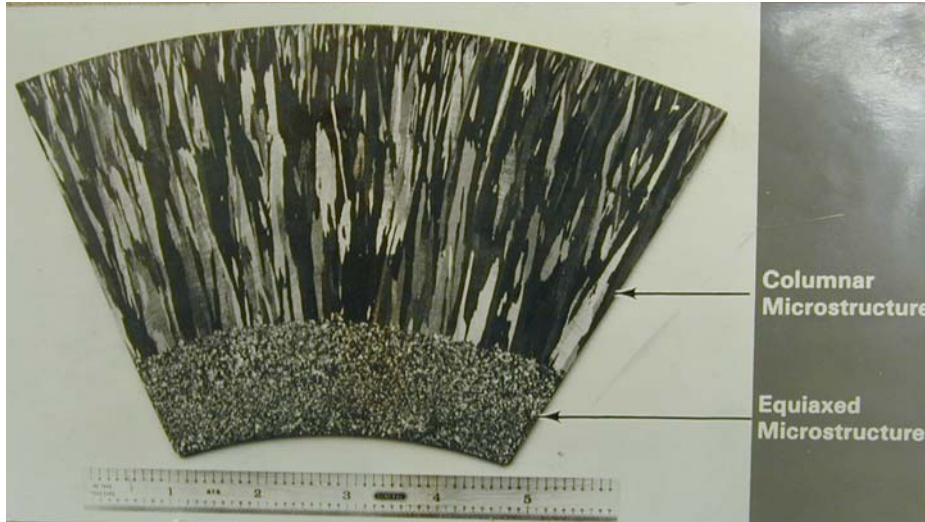
Figure 2.1. Example of Mixed Columnar and Equiaxed Microstructures (Specimen CCSS-EL-EQ-PNL-4)
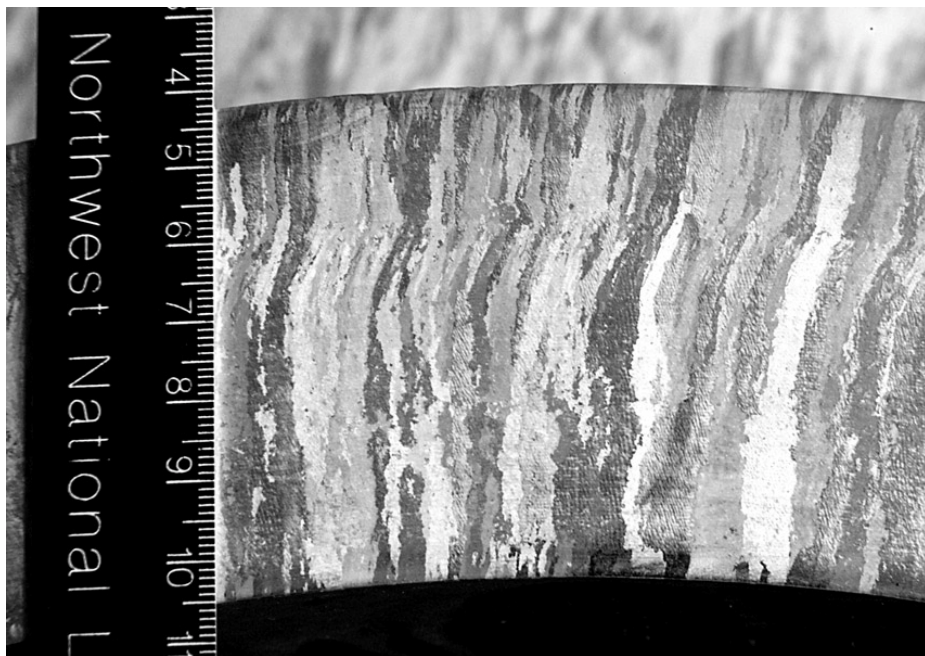
Figure 2.2. Photograph of Polished and Chemically Etched Surface of 8-cm-Thick Spool Piece Showing Bands of Columnar Grains and Bands of Equiaxed Grains (Specimen courtesy of Westinghouse Inc.)
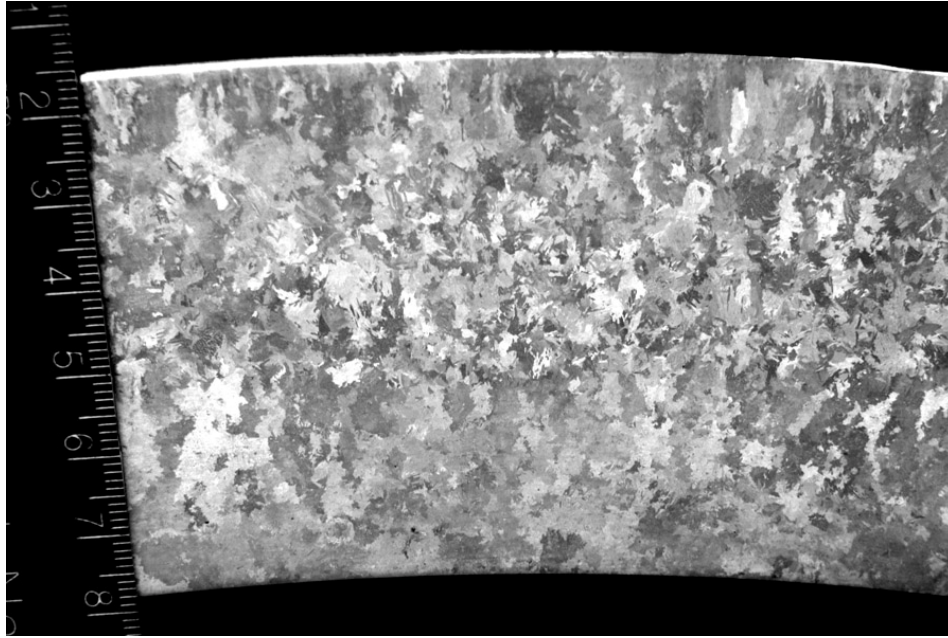
Figure 2.3. Example of Equiaxed Microstructure (Specimen courtesy of EPRI)

2.2   Material-Ultrasonic Interactions Common to CASS

Material-ultrasonic interactions are the basis for obtaining more meaningful NDE inspections, better characterization of materials, and can potentially guide the selection and optimization of inspections. CASS common to nuclear power plants is elastically anisotropic and polycrystalline. Interaction of ultrasonic waves with such material exhibits phenomena that are different than for isotropic or quasi-isotropic material. These include sound speed variations, ultrasonic beam deviation, high attenuation and high background acoustic noise caused by scattering, and phase variations across a wave front.

The choice of the wave mode significantly impacts ultrasonic inspection of CASS. Longitudinal (L) wave probes are now commonplace due to intractable issues of ray skew, backscatter, and attenuation inherent to vertically polarized shear (SV) waves when used in coarse-grain material or strongly textured material. However, the use of shear waves, while relatively uncommon in these materials, should not be disregarded for inspection and material characterization. The great majority of work documented in the literature addresses inspection in CASS. Very little exists concerning practical compensation of the material-ultrasonic effects common to CASS (Jeong 1987), although the use of ray tracing to increase the accuracy of anomaly location (Jeong and Ammirato 1989) has been proposed. A better understanding of CASS-ultrasonic interactions is necessary to address some of these problems.

BA Auld (1973) provides a general discussion of acoustic propagation within anisotropic material and derives slowness (inverse velocity) relationships for longitudinal waves, vertically polarized shear waves, and horizontally polarized shear (SH) waves. Figure 2.4 and Figure 2.5 are velocity surface and energy-ray deviation versus propagation angle estimates for a columnar grain stainless steel based on a hexagonal or transversely isotropic material model (Kupperman et al. 1981). An important observation is the percentage of sound speed change for a wave mode (Figure 2.4). Longitudinal wave and horizontally

polarized shear wave sound speeds vary a relatively small percentage as a function of orientation with respect to the crystal axes. The vertically polarized shear wave sound speed, however, varies by a large percentage as a function of orientation with respect to the crystal axes. Similarly, beam skew is relatively small for L and SV probes and large for the pure SH wave. Table 2.1 lists beam deviation or skew for common ultrasonic inspection probes (Kupperman et al. 1987). Figure 2.6 shows nomenclature for Table 2.1. Note that beam skew is small for longitudinal wave probes and large for shear wave probes. Similar sound speed and energy-ray deviation calculations are provided by Jeong (1987). Changes in sound speed and beam skew caused by pockets of a given microstructure clearly alter response location, if under the assumption of isotropic behavior, and can lead to misinterpretation. One might also argue that for a severe case, beam deviation might lead to the presumption that a material volume of interest was 100% inspected, but in actuality a given material volume may have been unintentionally skipped due to beam skewing around it.

Acoustic attenuation is a signal loss mechanism that consists of scattering and absorption. The former is proportional to the cube power of grain diameter and the fourth power of frequency for the Rayleigh regime where grain diameter or size is much smaller than the wavelength (Goebbels 1980). As a result, an ultrasonic noise baseline is typical of austenitic stainless steel inspection. For large grains, which are common to CASS material, scattering may extend beyond the Rayleigh regime and enter the
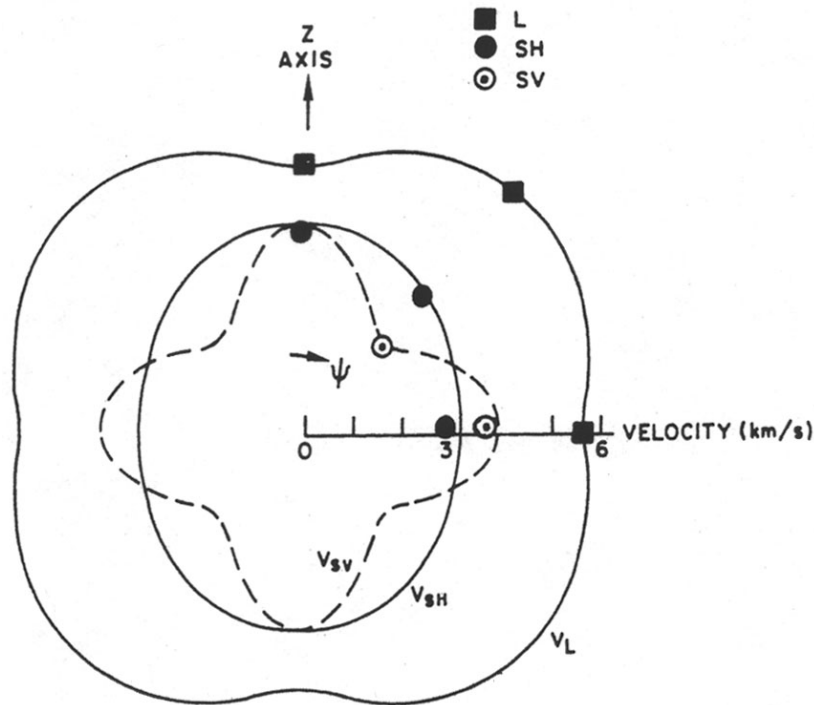
Figure 2.4.   Velocity-Surface Intersection with the (110) Plane for Columnar Grain Structure of Type 304 Stainless Steel. ψ is propagation angle relative to the columnar grain axis. Curves represent calculated results for the L, SH and SV mode sound waves; symbols indicate experimental data for Type 308 SS weld-metal samples (from Kupperman et al. 1981).
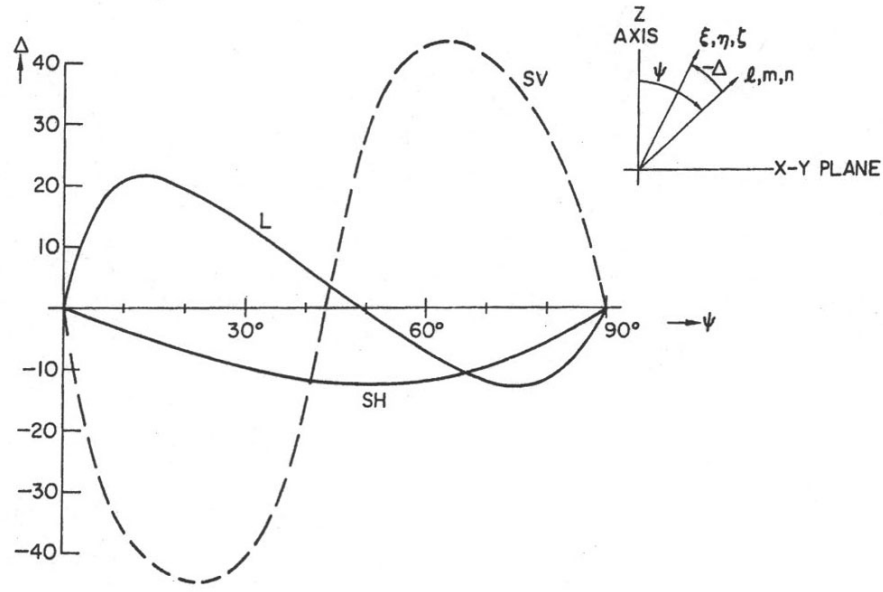
Figure 2.5. Energy-Ray Deviation (Δ) vs. Propagation Angle Relative to Columnar Grain Axis (ψ) in the (110) Plane for Columnar Grain Structure of Stainless Steel (from Kupperman et al. 1981).
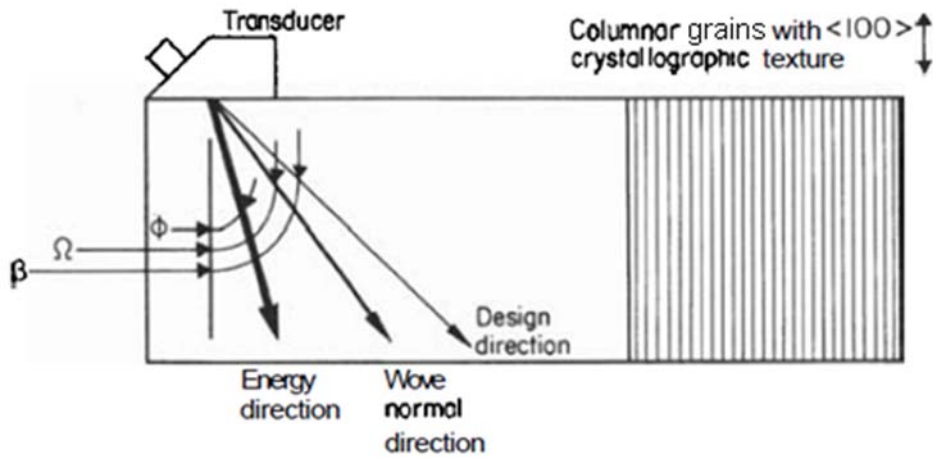
Figure 2.6. Schematic of Energy Flux Direction in Cast Stainless Steel. β is direction for which transducer was designed to propagate. Ω is actual direction of wavefront normal in columnar grain SS and φ is direction of propagation of ultrasonic energy (from Kupperman et al. 1987).

Table 2.1.　Propagation Direction of Wavefront Normal and Direction of Energy Flux in Columnar Grained Stainless Steel for Selected Ultrasonic Transducers (from Kupperman et al. 1987)

Transducer	Direction of Wavefront Normal (Ω)	Energy Direction Angle (φ)
45°S	35°(S)	4°(S)
60°S	42°(S)	36°(S)
70°S	47°(S)	64°(S)
45°L	49°(L)	49°(L)
	22°(S)	−22°(S)
55°L	62°(L)	53°(L)
	25°(S)	−18°(S)
70°L	72°(L)	60°(L)
	26°(S)	−16°(S)

stochastic and geometric regimes, depending on the wave frequency and wave mode. The use of low frequencies increases the ratio of wavelength to grain size and provides the following enhancements:

- Moves material-ultrasonic interactions toward a regime of quasi-isotropic behavior,

- Decreases interference from ultrasonic backscatter, and

- Increases penetration because the scattering portion of attenuation is reduced.

A tradeoff to low frequency inspection, however, is decreased spatial resolution. Fortunately, cast components are large and such a tradeoff is typically permissible within limits.

　　Another phenomenon common to CASS is ultrasonic beam distortion or phase distortion of a wave front. An illustration of the beam distortion effect is provided in Figure 2.7, which shows model predictions of the effect of sound speed variations within a heterogeneous polycrystalline material. The three runs correspond to sound speed variations from grain-to-grain of 0%, 1%, and 3% for the respective model predictions. Input parameters are a 2.4-mm grain size and a 5-MHz frequency with a focus at a 3.84 cm depth (Thompson et al. 2008). Beam distortion is evident for the 3% sound speed variation run. Similar studies showed that little beam distortion seems to exist for a 500-kHz shear wave in either equiaxed-grain CCASS or columnar-grain CCASS; however, high beam distortion is apparent for 1-MHz waves. Similarly, little beam distortion seems to exist for a 500-kHz longitudinal wave in equiaxed-grain CCASS, while a lens effect appears for columnar-grain CCASS due to the ray deviation or skewing effect. Moderate distortions exist at 2 MHz (Good et al. 1991). The doubling of the frequency for shear wave to longitudinal wave measurements attempts to keep the wavelength-to-grain size constant for comparing shear wave and longitudinal wave data. The longitudinal wave is less distorted than the shear wave in CCASS for roughly the same wavelength-to-grain size ratio.
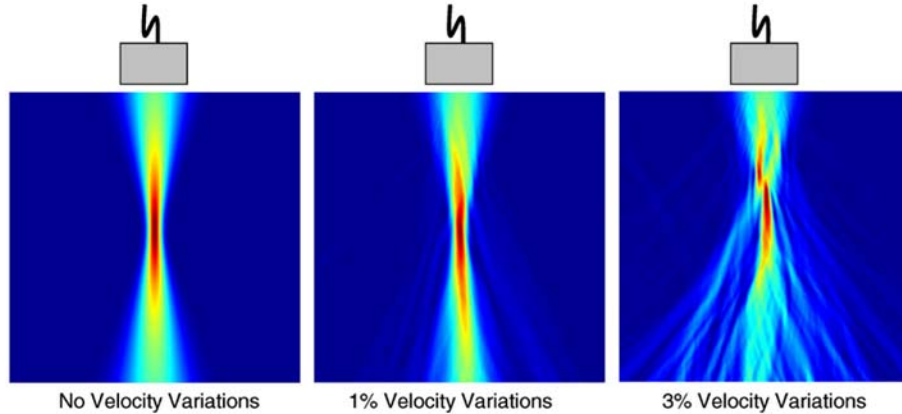
Figure 2.7. Distortion of a 5-MHz Continuous-Wave Gaussian Beam by an Inhomogeneous Medium (from Thompson et al. 2008)). Left: incident beam, focused at center (3.84-cm depth) of the domain and having a half width of 0.778 cm at the focus. Center: distortion produced by ±1% velocity variation. Right: distortion produced by ±3% velocity variation. The simulation assumes a microstructure consisting of cubic "grains," and though not representative of true equiaxed microstructure, provides a first approximation to distortion induced by velocity variations in individual grains.

For the case where multiple scattering becomes apparent, a strong distortion of the ultrasonic wave occurs due to scattered waves interfering with the primary or incident wave. This can lead to degradation and even loss of focusing of the wave (Bordier et al. 1991).

The phenomena discussed above have a deleterious effect on the ultrasonic signal from CASS specimens. However, they can form the basis for measurements that can classify microstructure of CASS components. In particular, measurements of ultrasonic attenuation and velocity have the potential to classify the microstructure of CASS components. These measurements are investigated further in this study. Other measurements based on phase mapping (Good et al. 1991), leaky surface waves[a] (Hildebrand et al. 1992), spectral analysis (Kumar et al. 2000), and diffuse backscatter (Ghoshal and Turner 2009) also appear to have potential.

2.3   Processing of Ultrasonic Signals from CASS Materials

High levels of background acoustic noise due to scattering from the grain boundaries are typical in the ultrasonic inspection of CASS specimens. Enhancing the SNR is therefore an important preprocessing step in the analysis of ultrasonic measurement data from CASS specimens (Hargreaves 1988). A brief review of signal processing techniques applicable to potential improvement of the ultrasonic SNR for CASS specimens is presented in this section.

Hargreaves (1988) discusses a variety of signal processing methods as applied to the analysis of data from CASS specimens. All signal processing techniques solely examined an RF signal consisting of the back-surface response of a specimen with a rectangular cross section. In some instances, signal

---

(a) Hildebrand BP, MS Good, and AA Diaz. 1991. *Ultrasonic Classification of Centrifugally Cast Stainless Steel Utilizing the Rayleigh Critical Angle Technique.* Technical Letter Report from PNNL to the NRC.

processing yielded an improved SNR but improvements were generally limited. An adaptive least squares filter technique yielded some improvement in the SNR when used with a broad bandwidth signal; however, such an improvement might not be applicable to narrower bandwidth transducers.

Other approaches to enhancing the SNR of ultrasonic measurements (although not necessarily from CASS specimens) have also been proposed. Spatial and frequency compounding (Bencharit et al. 1986; Choi 2007) methods use weighted averages of several measurements to improve SNR. Deconvolution methods assume a linear model for each of the measurement subsystems, and attempt to compensate for their effect on the measured data. Deterministic deconvolution techniques that assume a convolving filter did not result in an improvement in SNR with model data, particularly for low amplitude responses from CASS specimens (Hargreaves 1988). Similar results were observed when deconvolution using a minimum phase filter was applied, and the most promising results were obtained by a minimum entropy deconvolution (MED) technique (Hargreaves 1988). Other studies have also indicated the potential for improvement in flaw detection through deconvolution, although not necessarily in CASS (Ghouti 1997). Wavelet and related time-frequency techniques have also been successfully applied to reduce speckle noise and enhance ultrasonic signal SNR in CASS inspection (Chen et al. 1999; Park et al. 2004).

Other methods, such as the split spectrum processing technique (Bilgutay et al. 1989; Shankar et al. 1989) as well as the more general class of synthetic frequency diversity algorithms (Ericsson 1994) also show some potential. Time-averaged mean and mean-squared values were effective when the back surface response was relatively strong but were relatively ineffective for low amplitude signals (Hargreaves 1988). However, split-spectrum based polarity thresholding (Shankar et al. 1989), either alone or in combination with other processing techniques such as minimization (Newhouse et al. 1985) appears to significantly improve detectability in CASS specimens. A maximum entropy model of spectral analysis also had limited success (Hargreaves 1988). Miralles et al. (2004) discuss the application of higher order statistics (HOS) for analyzing ultrasonic backscatter. Though the focus of the work is on classifying scatterer (or grain) sizes based on HOS, similar approaches may potentially be applied to improve SNR or characterize microstructure. The use of nonlinear homomorphic filters (Morris et al. 1995) for reducing distortion and improving the imaging of strong scatterers have also been proposed. Note that SAFT techniques for CASS inspection (Silverstein and Thomas 1993; Anderson et al. 2007) also make use of signal processing tools to improve the beam-forming capabilities and reduce clutter.

3.0   Experiments

The discussion in the previous section highlights the possibility of using ultrasonic measurements for in-situ characterization of CASS microstructure, and ultrasonic experiments were designed to test this hypothesis. A two-class discriminant problem was postulated where CASS macrostructure was either equiaxed-grain or columnar-grain material. If data and analysis provided a means to successfully sort material into these two classifications, then justification to develop a more thorough and staged exploration would exist. The two ultrasonic measurements proposed for the experiment were time-of-flight ratio of a normal incidence shear wave to a normal incidence longitudinal wave, and longitudinal wave attenuation. Metallographic measurements were also acquired to provide insight on specimen macrostructure and microstructure. Details of these measurements are provided in this section.

3.1   Centrifugally CASS Specimens

Six specimens (Figure 3.1) were selected from an assortment of PNNL samples that had been previously used in PNNL studies as well as for Action 4 of the Programme for the Inspection of Steel Components III (PISC III). The PISC III specimens consisted of a welded pipe section with a girth circumferential weld joining two pipe sections of equiaxed grain and columnar-grain material, respectively (Figure 3.1 and Figure 3.2). A stamped label (B510, B511, B515, B516, B517 and B527) uniquely identified each specimen. Destructive analysis of a 1-cm thick section from Specimen B515 (Figure 3.1) was conducted to obtain metallographic measurements. The remaining five specimens (consisting of a total of five material volumes of equiaxed-grain material and five volumes of columnar-grain material) were used to obtain both ultrasonic time-of-flight and attenuation measurements. Typical axial, radial, and circumferential arc length dimensions of a specimen were 40 cm, 5.9 cm, and 18 cm, respectively. Pipe wall thickness of the columnar material typically ranged between 59.9 and 60.5 mm while that of the equiaxed material typically ranged between 57.7 and 57.9 mm.
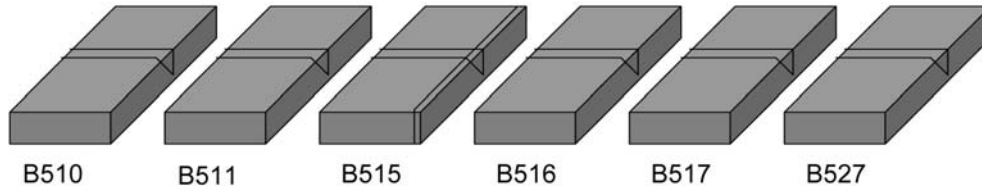
Figure 3.1.   Selected PISC III Specimens Used for Metallurgical or Ultrasonic Measurements. Specimens B510, B511, B516, B517, and B527 were used for ultrasonic measurements. A 1-cm thick slice was removed from the side of Specimen B515 for metallographic analysis. Each specimen is a welded assembly of two pipe sections where one material was an equiaxed material and on the opposite side of the weld was a columnar material.
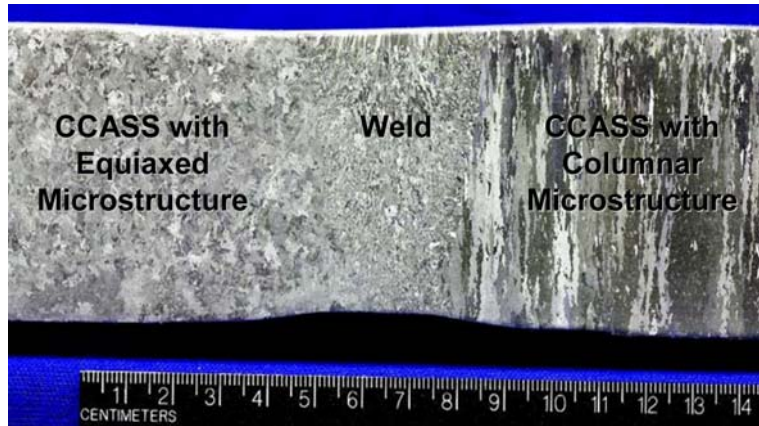
Figure 3.2. A Representative Axial-Radial Cross Section of a CCASS Specimen, Showing Typical Outside and Inside Diameter Geometry, and Microstructure of a Specimen. The equiaxed CCASS grains on the left have a mean lineal intercept of 2.3 mm and the columnar CCASS grains on the right have a mean lineal intercept of 2.5 mm. The mean lineal intercept is the average length of a line segment that crosses a sufficiently large number of grains. It is proportional to the equivalent diameter of a spherical grain (Steele and McCall 1984).

3.2   Metallographic Characterization

3.2.1   Specimen for Metallographic Analysis

A 1-cm-thick section was removed from Specimen B515 and sacrificed for destructive analysis to obtain metallographic measurements. Appendices A and B document the results of this analysis. A brief summary is provided below.

3.2.2   Metallographic Analysis

The texture and microstructure of material removed from CASS Specimen B515 was characterized using scanning electron microscopy (SEM) and electron backscatter diffraction (EBSD) analysis as shown in Figure 3.3 and Figure 3.4. The material volume was labeled as an axial-radial cross section of Specimen B515. The purpose was to understand the microstructural variations from the two regions on either side of the weld joint. The grain structure and overall texture were explored using EBSD, which is a technique that directly measures the orientation at any point within a grain that is excited by the electron beam (100–300-nm-diameter probe) in the scanning electron microscope. Scanning revealed that a strong orientation was present for the "Columnar Grain" material, with alignment along the radial (Y-) direction and a weaker alignment equally distributed in the axial (Z-) and transverse or circumferential (X-) directions as shown in Figure 3.3. Data suggested that during the casting process a few grains dominated the growth into the liquid melt during solidification after approximately 10 mm from the outside surface of the piping. Scanning of the "Equiaxed Grain" material revealed a fine equiaxed dendritic microstructure that exhibited a texture. Figure 3.4 suggests that taken as a whole, this region doesn't have a singular orientation. However, further analysis (Appendix A) revealed that the dendritic colonies had a preferred alignment at a 38° angle to the Y-direction (radial direction) which had not been anticipated. Appendices A and B present additional analyses of the two regions.

12
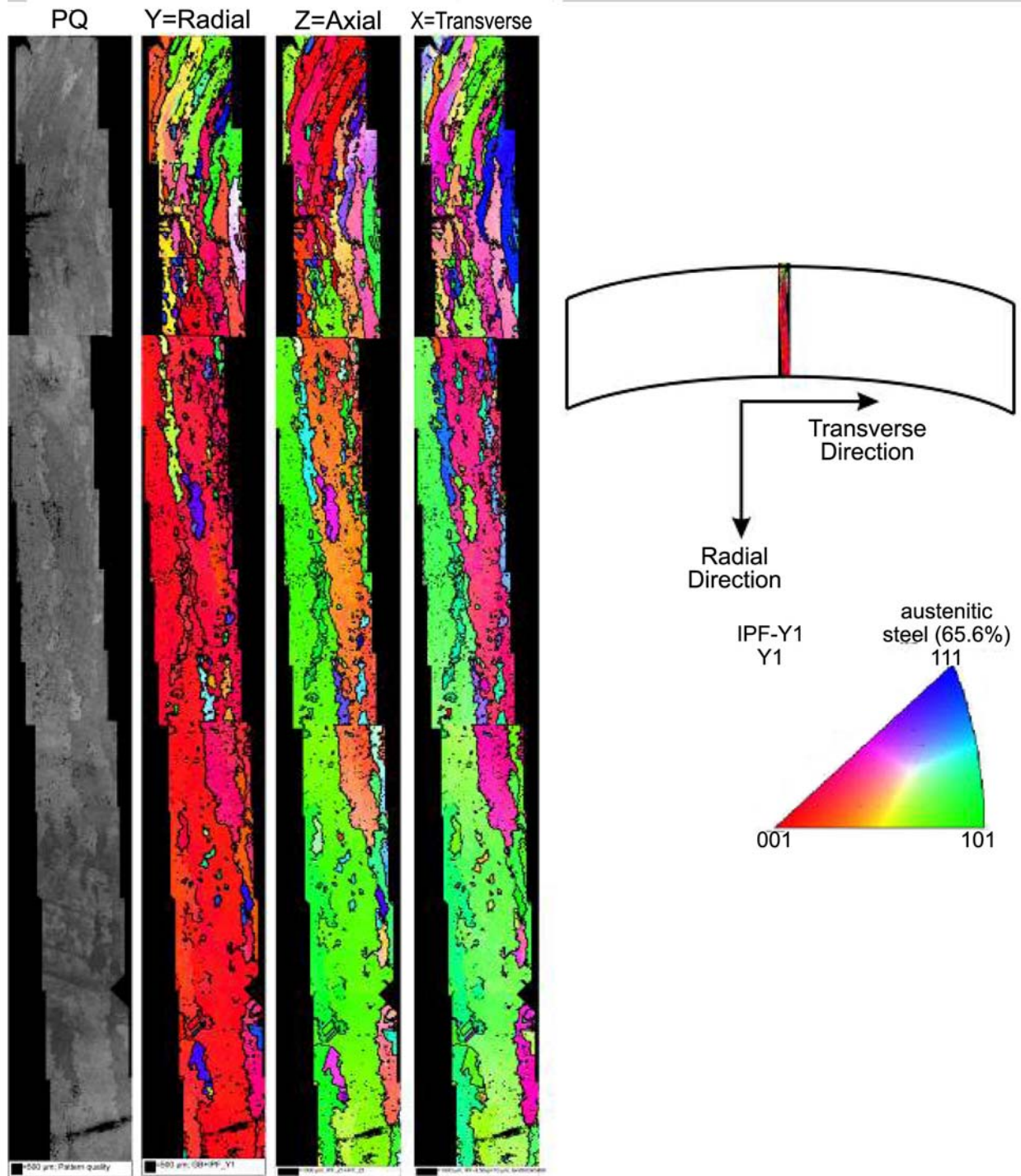
Figure 3.3. Characterization of "Columnar Microstructure" Area of Specimen 515 by a Pattern Quality Map and the Three Inverse Pole Figure Maps in the y, z and x Directions. Each color map shows the orientation of each region as viewed from the indicated direction. Y is the vertical or radial direction, Z (axial direction) is normal to the page, and X is the horizontal or transverse direction.
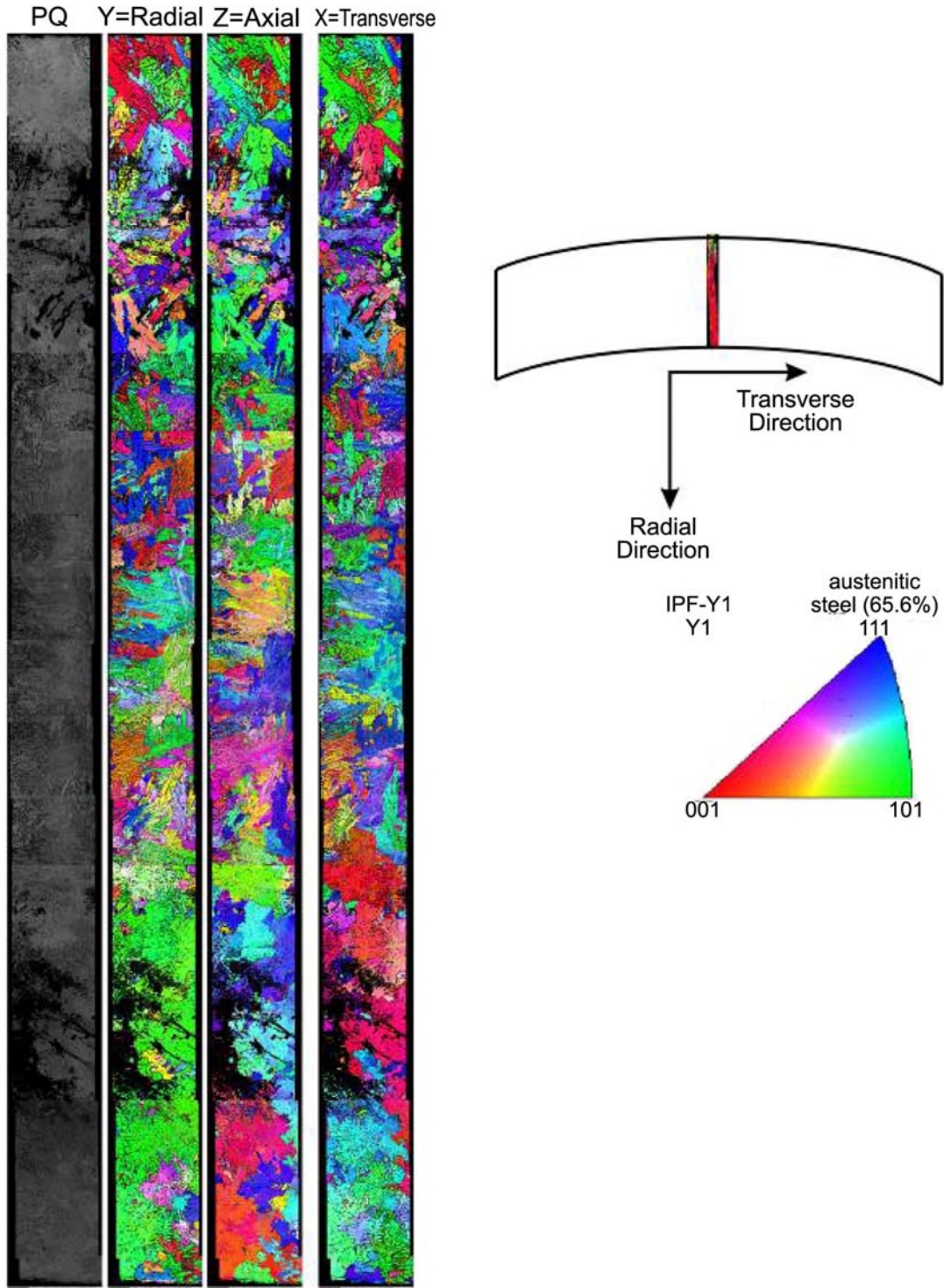
Figure 3.4. Characterization of "Equiaxed Microstructure" Area of Specimen 515 by a Pattern Quality Map and the Three Inverse Pole Figure Maps in the Y, Z and X Directions. Each color map shows the orientation of each region as viewed from the indicated direction. Y is the vertical or radial direction, Z (axial direction) is normal to the page, and X is the horizontal or transverse direction.

Figure 3.5. Two Locations Selected for Placement of Longitudinal Wave Transducer and Shear Wave Transducer. Circles equivalent to the transducer diameter were marked on the outer diameter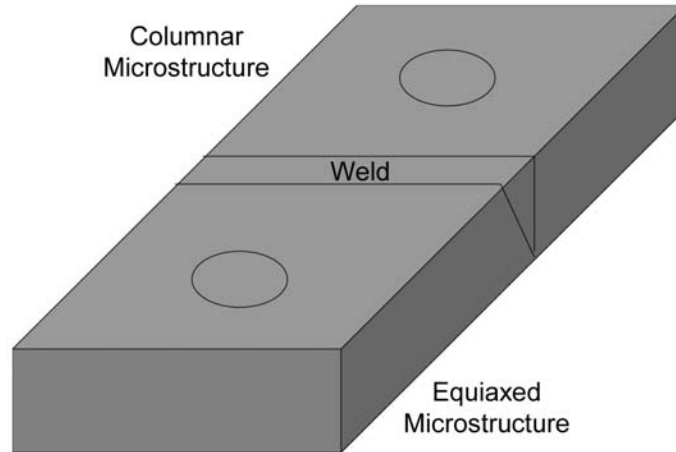 (OD) surface to aid transducer placement so longitudinal and shear wave data was acquired from the same material volume for a TOFRSL ratio value. If an inner surface feature was observed, locations were shifted away to avoid interference.

3.3   Ultrasonic Time of Flight Ratio

The first parameter measured was a time-of-flight ratio of a normal incidence shear wave to that of a normal incidence longitudinal wave (TOFRSL). A TOFRSL measurement was selected because the technique eliminates the need to have thickness data that typical sound speed measurements require.

3.3.1   Transducer Placement for TOFRSL Measurements

Two transducer locations were selected from each specimen, with one for the equiaxed material and the other for the columnar material (Figure 3.5). Surface anomalies such as gouges were detected by visual or tactile inspections and marked. Selected transducer locations were centrally located within the respective material type to avoid edge effects and avoided detected surface anomalies.

3.3.2   TOFRSL Experimental Setup

The TOFRSL experimental setup used a RITEC (RITEC, Inc., Warwick, Rhode Island) square-wave pulser (model SP-801), broadband receiver (model BR-640), diplexer (RDX-2), a LeCroy (LeCroy Corporation, Chestnut Ridge, New York) oscilloscope (model WaveRunner® 64Xi), and two ultrasonic transducers. The ultrasonic transducers were employed to generate normal incidence, shear waves, and longitudinal waves. Both were Olympus NDT, Panametrics transducers - model V391 [2.86-cm (1.125-in.) diameter, 500-kHz, longitudinal wave transducer] and model V151 [2.5-cm (1.0-in.) diameter, 500-kHz, shear wave transducer] and were unfocused. An ultrasonic couplant gel and a 3–5-minute-setting epoxy (DOUBLE/BUBBLE® Hardman® Structural Adhesives, Royal Adhesives & Sealants, LLC, Belleville, New Jersey) were respectively used as longitudinal wave and shear wave couplants with the transducer applied directly to a selected location on the outer diameter surface. The Bayonet Neill-Concelman (BNC) connector of the shear-wave transducer was oriented parallel to the pipe specimen

axes to maintain a consistent shear wave polarization with respect to the specimen and microstructure. The shear-wave measurement was acquired approximately 50 minutes after mixing the epoxy.

3.3.3   TOFRSL Data Analysis

Ten qualitative TOFRSL values were estimated; that is, a value for equiaxed material and a value for columnar material for each of the five specimens (Figure 3.6). A zero-crossing technique was used to determine TOF measurements. Corresponding zero-crossing features were used for the back surface response and the second occurrence of the back surface response of the longitudinal wave to measure the time interval. The shear wave TOF measurement was the time interval between the ultrasonic trigger and a zero-crossing feature from the back surface response. This was due to poor signal quality of the second occurrence of the back surface response. Figure 3.6a presents the normal incidence longitudinal and shear wave TOF measurements as a scatter plot. The calculated TOFRSL value for all of the specimens is shown in Figure 3.6b.

3.3.4   TOFRSL Results

The TOFRSL data show a cluster of values around 1.6 for columnar-grain material and another cluster around 2.0 for equiaxed-grain material with no overlap between the two classifications (Figure 3.6b). Furthermore, the separation between the mean values of the two classifications (1.62 and 2.02 for columnar and equiaxed microstructures, respectively) was large relative to the standard deviation of either classification (0.04 and 0.05 for columnar and equiaxed microstructures, respectively). The estimated values were also offset relative to expected TOFRSL values of 1.4 and 1.7 for columnar-weld metal and equiaxed-grain material reported by Kupperman et al. (1987). Overall, the TOFRSL values appear to provide a nondestructive means to classify CASS material as either equiaxed-grain or columnar-grain material based on a simple threshold criteria. However, the experiment was performed once and additional measurements are needed to demonstrate repeatability. Further, data from one columnar and one equiaxed sample appear to be outliers and need further investigation.

3.4   Longitudinal Wave Attenuation

A qualitative evaluation of longitudinal wave attenuation was selected for investigation because theory predicts higher attenuation for a normal incidence wave in equiaxed-grain material and lower attenuation for columnar-grain material (Ahmed and Thompson 1995). One basis for this difference in attenuation is that a higher density of grain boundaries exists along the radial axis of the pipe for equiaxed-grain material relative to columnar-grain material. Other phenomena (such as the acoustic lens effect caused by beam skew that occurs for columnar-grain material) may also impact the measured attenuation. However, the contribution of these phenomena to the total attenuation was assumed to be small in comparison to the contribution from scattering at the grain boundaries.
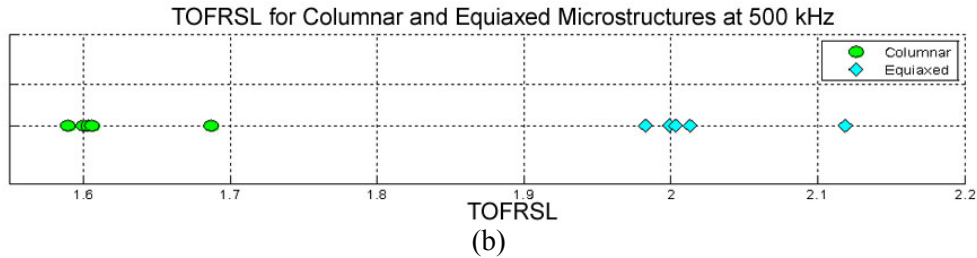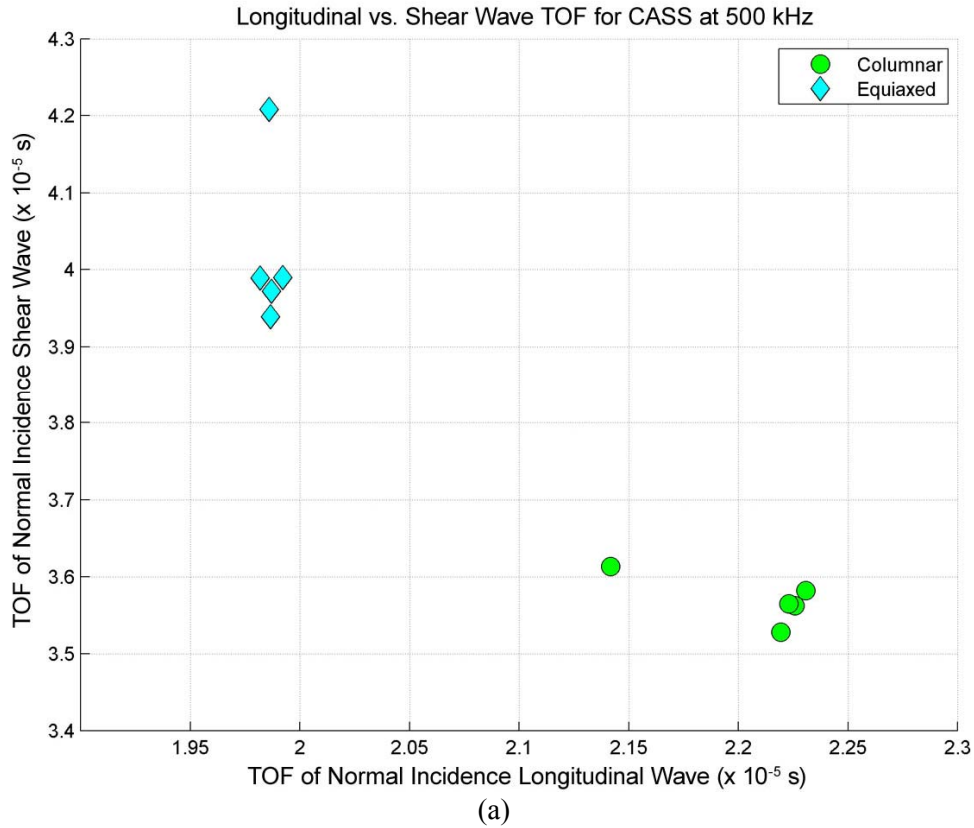
Figure 3.6. (a) Scatter Plot of Longitudinal Wave TOF Against Shear Wave TOF. (b) Qualitative Time-of-Flight Ratio of Normal Incidence Shear Wave to Normal Incidence Longitudinal Wave Measurements

3.4.1 Transducer Placement for Attenuation Measurements

Twelve locations were selected from each of the five specimens for the attenuation measurements. Of the twelve locations on a single specimen, six were from the equiaxed-grain material and six from the columnar-grain material. The 12 transducer locations were selected to minimize edge effects and avoid regions affected by surface anomalies. A typical layout is shown in Figure 3.7 with a slight overlap between interrogated material volumes. If surface anomalies had been detected, the area overlap between transducer locations was increased to enable six measurements over a smaller usable area defined by the exclusion of surface anomaly regions. In all cases, an area overlap no greater than 50 percent existed between any two locations.

17
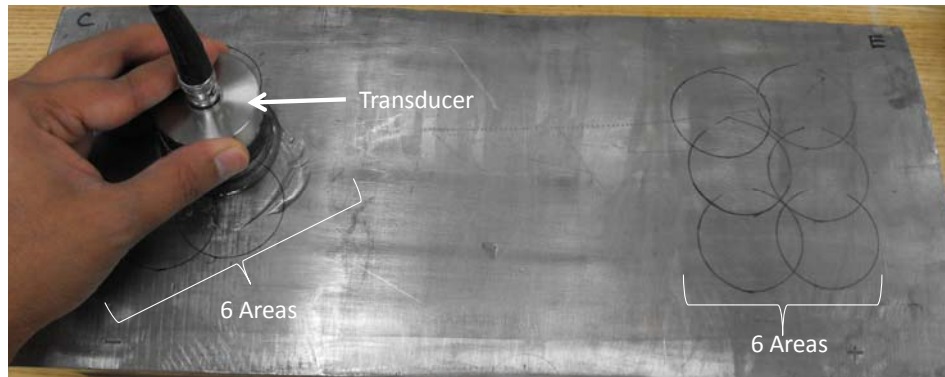
Figure 3.7. Twelve Locations Selected for Placement of Longitudinal Wave Transducer. Circles equivalent to the transducer outer case diameter were marked on the outer diameter surface to document transducer placement. If a surface feature was detected, locations were shifted to avoid interference but with the tradeoff of increased area overlap between areas. No two areas had an overlap greater than 50 percent.

3.4.2   Longitudinal Wave Attenuation Experimental Setup

The experimental setup for measuring attenuation is shown in Figure 3.8, and used the same measurement equipment as in the TOFRSL setup. An Olympus NDT, Panametrics A392S transducer, with center frequency around 1 MHz and 3.81-cm (1.5-in.) diameter was used as the probe. The attenuation calculations were also repeated using data from a Panametrics V391, 500-kHz transducer with diameter 2.86 cm (1.125-in.).

In each case (1-MHz and 500-kHz transducers), the transducer was placed in contact with the specimen, with a thin layer of ultrasonic gel couplant to ensure proper coupling of energy to the specimen. The instrument settings for the pulser, receiver, and diplexer were held constant throughout the experiment. In particular, the gain on the receiver was held constant (60 dB when using the 1-MHz transducer, 64 dB when using the 500-kHz transducer) regardless of whether the material being inspected was columnar or equiaxed. This enables a direct comparison of the measurement data from each region. The transducer contact was manually adjusted to maximize the received signal voltage, while 64 consecutive signals were averaged to minimize the effect of electronic noise. A LeCroy (model WaveRunner® 64Xi) digital oscilloscope was used to perform the averaging, and to digitize and save the signals. The time gate (and delay) was selected to ensure that each signal showed at least two back-wall reflections (Figure 3.8). The averaged signal was sampled at 500 MHz, and the samples saved and exported to the MATLAB software package (Version R2009a) for analysis.

A. Transducer on CASS specimen
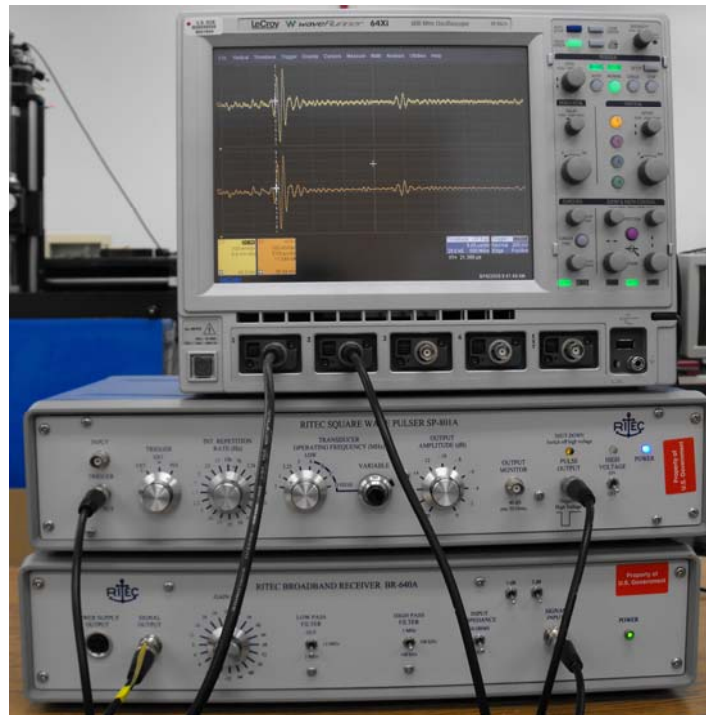
B. Example of signal from CASS specimen

Figure 3.8. Instrumentation Used for Longitudinal Wave Attenuation Experiment. The bottom trace on the oscilloscope shows the RF signal after averaging of 64 waveforms. The first two back-wall reflections are seen in the traces. Data was sampled at 500 MHz and exported to the MATLAB software for analysis.

3.4.3   Longitudinal Wave Attenuation Data Analysis

Estimates of attenuation from the raw measurements will be somewhat higher than the true value, due to the effect of transducer beam-spreading (or ultrasonic diffraction). Therefore, a correction for ultrasonic diffraction is necessary to address this effect. The attenuation coefficient α can be computed using two consecutive ultrasonic back-wall reflections as shown in Eq. (3.1):

$$\alpha = \frac{\log_e(\rho) - \log_e\left(\left\|\hat{V}_2(\omega) \middle/ \hat{V}_1(\omega)\right\|\right)}{2D} \tag{3.1}$$

where ρ is the magnitude of the reflection coefficient, D is the thickness of the specimen, $\hat{V}_1(\omega)$ is the diffraction-corrected first back-wall reflection, and $\hat{V}_2(\omega)$ is the diffraction and phase-corrected second back-wall signal as a function of angular frequency ω. The phase correction for the second back-wall signal compensates for the propagation delay between the first and second back-wall signals. The division of the two reflection signals in the frequency domain compensates for the instrumentation and transducer responses. A detailed derivation of this equation is presented in Appendix C. The attenuation in Eq. (3.1) is in Nepers per meter, and can be converted to dB/m by using

$$\alpha \text{ in dB/m} = 8.686 \times \alpha \text{ in Np/m}$$

The diffraction correction term requires knowledge of the specimen thickness, as well as the wavelength (or equivalently, the ultrasonic wave velocity) in the material (see Appendix C for details). The specimens tested in this study were of different thicknesses (corresponding to slightly different ultrasonic path lengths for the first and second back-wall reflections). In addition, the results from the TOFRSL experiment indicate small differences in the longitudinal wave velocity as well. To account for these differences in thickness and velocity, the ultrasonic time-of-flight (measured from the RF signals as the time delay between the two successive back-wall reflections) and the sample thickness (measured on the specimen) was used in the diffraction correction computation. Note that this may not be feasible in a field examination, where thickness values may not be accurately known or reported. Figure 3.9a presents the computed beam profile on the axis of the transducer, as a function of distance (in meters), at an inspection frequency of 1 MHz. The near field length for the (3.81-cm diameter) transducer that was used, as well as the distance corresponding to the first and second back-wall reflections for one of the specimens, is indicated on the figure. From this figure, it is seen that both reflections are in the far field region (though the first reflection is just within the far field region). Similar results were obtained on other specimens. The magnitude of the diffraction correction term as a function of normalized distance, $z\lambda/a^2$, for one of the specimens, is presented in Figure 3.9b. Again, the normalized distances corresponding to the first and second back-wall reflections, at an inspection frequency of 1 MHz when using a 3.81-cm diameter transducer, are also shown in the figure. Similar results were obtained from the 2.86 cm diameter, 500-kHz transducer (Figure 3.10). The calculations indicate that the diffraction correction term in this experiment is not insignificant (at least at 1 MHz), and must be accounted for when estimating the attenuation. Further, the calculated correction for ultrasonic diffraction based on the transducer and nominal thickness of the specimen was very similar for the different specimens (for both columnar and equiaxed grain structure). Thus, the correction term may potentially be pre-computed (depending on the transducer and nominal thickness of the specimen) for field use, without resulting in a large error.

Note that, since the correction terms are in terms of normalized distance, they can also be interpreted as correction terms for different wavelengths, if the ultrasonic path lengths are held constant. Figure 3.11a shows the correction as a function of frequency, for the 1 MHz transducer, while Figure 3.11b presents similar information for the 500-kHz transducer. In both figures, the ultrasonic path

length corresponds to twice the specimen thickness. These frequency-domain correction terms are used to compute $\hat{V}_1(\omega)$ and $\hat{V}_2(\omega)$ in Eq. (3.1).

From Eq. (3.1), it is clear that the data from the two back-wall reflections need to be processed in the frequency domain. However, direct division of the two frequency-domain signals will result in problems because of the presence of noise. Therefore, the compensation is carried out using the Wiener deconvolution algorithm (Gonzalez and Woods 1999). An overview of the Wiener deconvolution algorithm is provided in Appendix C.

A step-by-step approach to calculating the attenuation using Eq. (3.1) is presented below.

1. Signal Extraction: This step identified the two back-wall reflections from each RF signal, and gated the raw RF signal around each reflection using an 8192-point gate (corresponding to a time-gate of 16.38 microseconds).

2. Signal Averaging: The gated first back-wall signals from a single region were averaged (spatial average) to reduce any residual effects due to improper coupling or location-dependent signal effects. Similarly, the second back-wall signals from the region were also averaged. This step resulted in a reduction in the number of signals (from six signals to one averaged signal per region), for a total of five signals from equiaxed regions and five from columnar regions.

3. Spectrum Estimation: Each averaged signal underwent mean-removal, windowing using a Hamming window, followed by a Fourier transform using the fast Fourier transform (FFT) algorithm. A 16384-point FFT was computed to increase the frequency resolution.

4. Compensation: Both back-wall spectra underwent diffraction correction using terms similar to those presented in Figure 3.11. The correction was implemented using a Wiener deconvolution procedure as discussed in Appendix C. In addition, the second back-wall spectrum was compensated for the propagation delay corresponding to two additional transits through the specimen thickness.

5. Deconvolution: This step removes the effect of the measurement equipment, and effectively computes a transfer function for the material. Again, the deconvolution was implemented using a Wiener deconvolution procedure.

6. Attenuation Estimation: The final step computes the attenuation using Eq. (3.1). Note that because the front surface reflection coefficient is not known precisely, the attenuation is only known up to a finite constant.
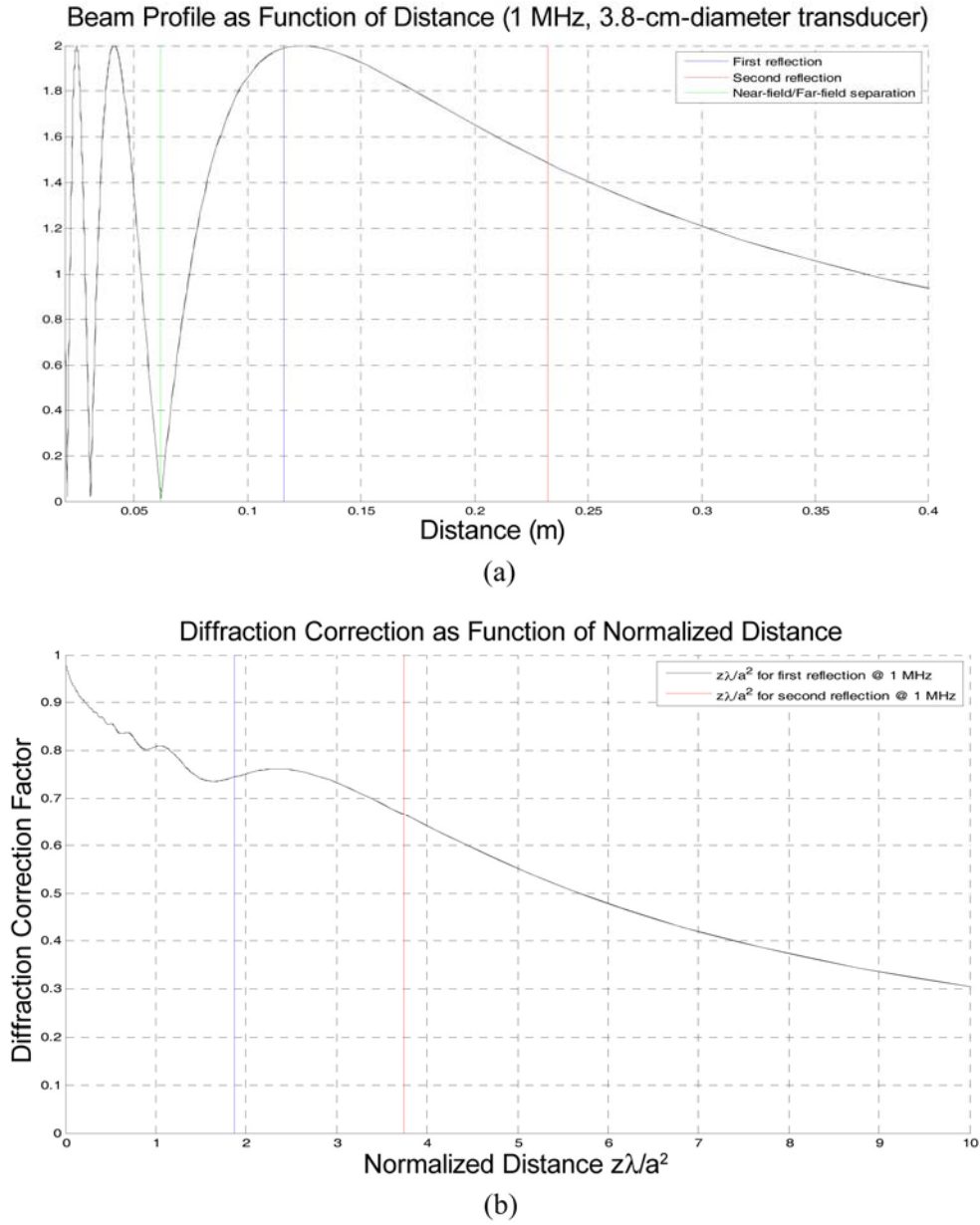
Figure 3.9. (a) Ultrasonic Beam Profile for a 1 MHz, 3.81-cm-diameter Transducer Showing the Near Field Length, and Distances of the First and Second Back-Wall Reflection. (b) Diffraction Correction as a Function of Normalized Distance. Normalized distances at 1 MHz, corresponding to the first and second back-wall reflection, are shown on the figure.
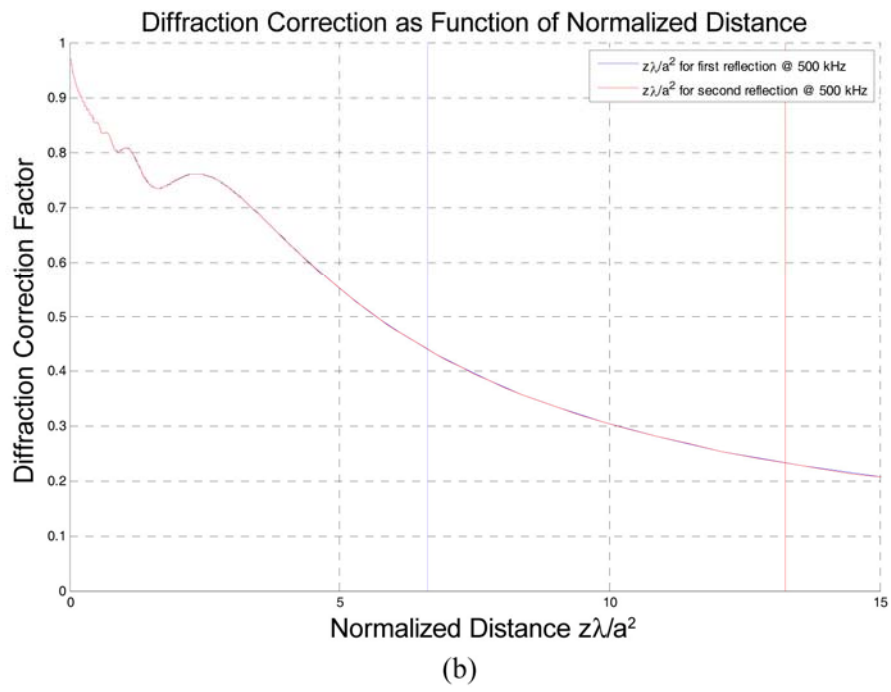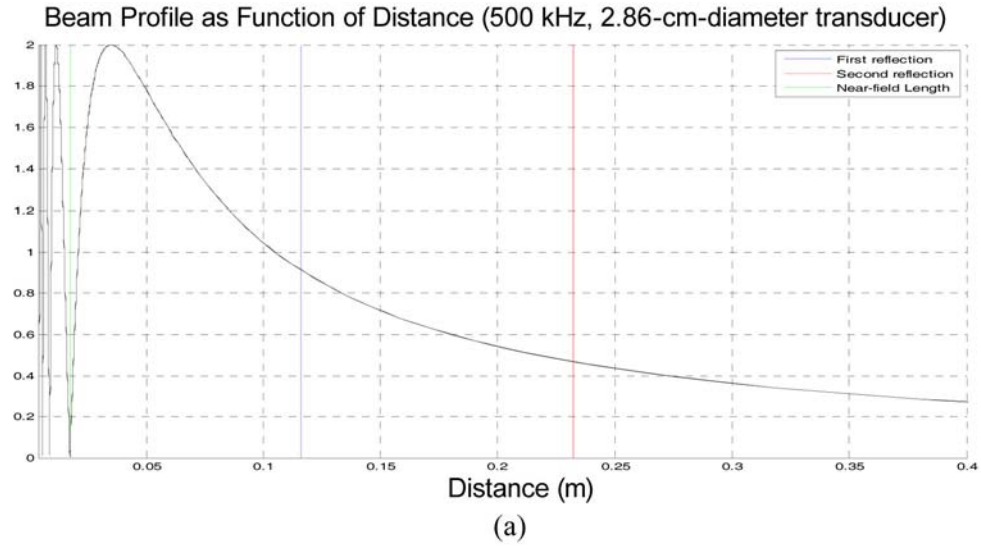
Figure 3.10. (a) Ultrasonic Beam Profile for a 500 kHz, 2.86-cm-diameter Transducer Showing the Near Field Length, and Distances of the First and Second Back-Wall Reflection. (b) Diffraction Correction as a Function of Normalized Distance. Normalized distances at 500 kHz, corresponding to the first and second back-wall reflection, are shown on the figure.
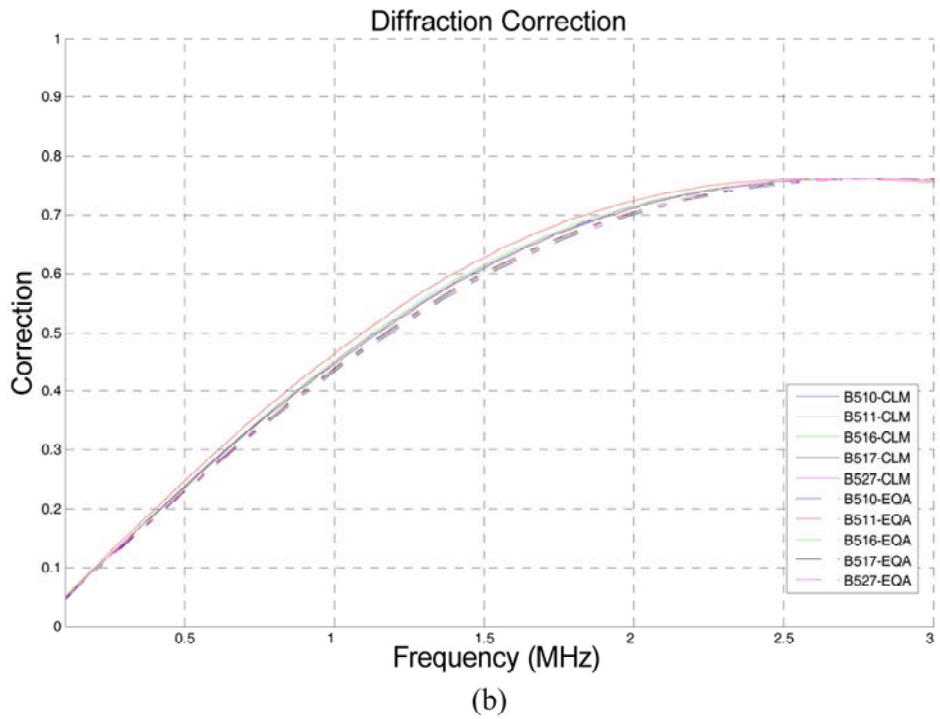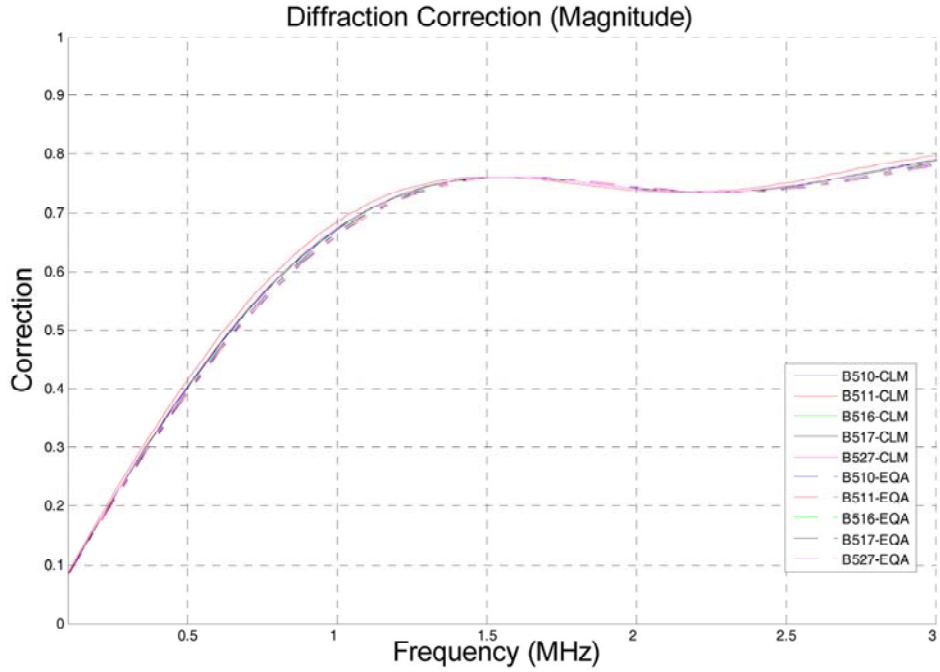
Figure 3.11. Diffraction Correction Presented as a Function of Frequency: (a) for the 1 MHz, 3.81-cm-diameter transducer, (b) for the 500 kHz, 2.86-cm-diameter transducer

### 3.4.4   Longitudinal Wave Attenuation Results at 1 MHz

The results of the calculations for the five specimens are provided in Figure 3.12–Figure 3.20. Figure 3.12 presents the raw time-domain signals for each of the 10 regions (5 equiaxed and 5 columnar). The signals are color-coded according to specimen ID (B510, B511, B516, B517, and B527). Signals from columnar regions are presented using solid lines while signals from equiaxed regions are presented using dashed lines. This (color and line-style) convention is followed in all the subsequent plots. A cursory examination of the data in Figure 3.12 shows that the signal amplitudes from the equiaxed region are substantially lower than those from the columnar region. Because the experimental parameters (such as applied energy and receiver gain) were not varied throughout the experiment, a possible explanation for this observation is that equiaxed grain structures attenuate ultrasonic energy more than columnar regions. However, the dissimilar thicknesses of the regions may mean longer path lengths in some specimens, which in turn can result in greater attenuation of the signal amplitude. Therefore, the estimation of the attenuation coefficient is necessary before any conclusions may be drawn.

Figure 3.13 presents the gated first back-wall reflection in the time domain, while Figure 3.14 shows the (FFT) magnitude spectrum. The magnitude spectrum was computed after all gated signals from a single region were averaged (after appropriate time shifts to ensure that the peaks of the signals were aligned). The frequency domain data are presented only between 100 kHz and 3 MHz, because this was the receiver bandwidth used in the experiments. At the low-frequency end (less than 100 kHz), a low-frequency baseline variation (due to insufficient damping) was observed that could not be filtered out in the receiver without losing the signals of interest. The baseline variation was reduced by the use of piece-wise linear trend removal; the use of filters to remove this baseline variation was not attempted in this study. Figure 3.15 and Figure 3.16 show the time and frequency domain information for the second back-wall reflection. The processing stages were identical (i.e., time gating, peak-alignment followed by averaging, windowing using a Hamming window, followed by FFT computation).

Figure 3.17 and Figure 3.18 show the magnitude and phase spectra, respectively, of the material transfer function after compensation and deconvolution. The phase spectrum is shown after unwrapping (i.e., absolute jumps greater than or equal to π radians have been replaced by their 2π complement). The data are presented between 800 kHz and 1.3 MHz because the magnitude of the transfer functions is significantly noisy outside this range (due to noise dominating in the deconvolution procedure). In most cases, the ratio of the energy in the second back-wall signal to that in the first back-wall signal is higher for columnar microstructure. The corresponding attenuation estimates are presented in Figure 3.19 (between 100 kHz and 3 MHz) and Figure 3.20 (focused on the range between 800 kHz and 1.3 MHz). From these figures, the attenuation in the columnar regions is seen to be lower than that in the equiaxed regions (by about 0.5–2 dB/cm). Data from one sample (B510-Columnar) is seen to exhibit attenuation characteristics that are between the columnar and equiaxed characteristics. This data (and sample) is being examined further to determine the cause of this variation.
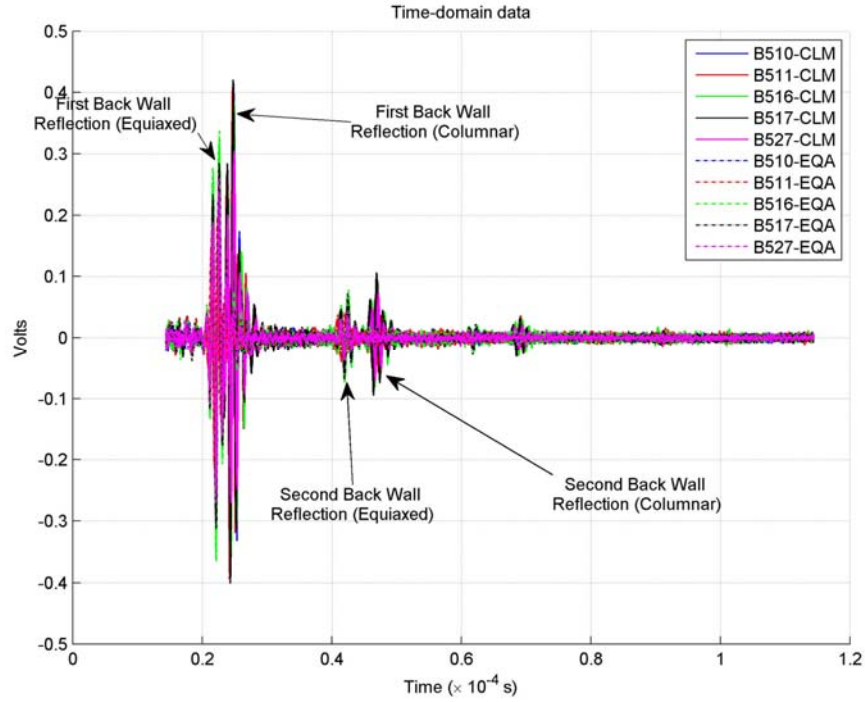
Figure 3.12. Ultrasonic Data (RF) from Columnar and Equiaxed Microstructure CASS Specimens in the Time Domain. The figure shows all the signals, from all specimens. The first and second back-wall reflection signals are indicated on the figure.
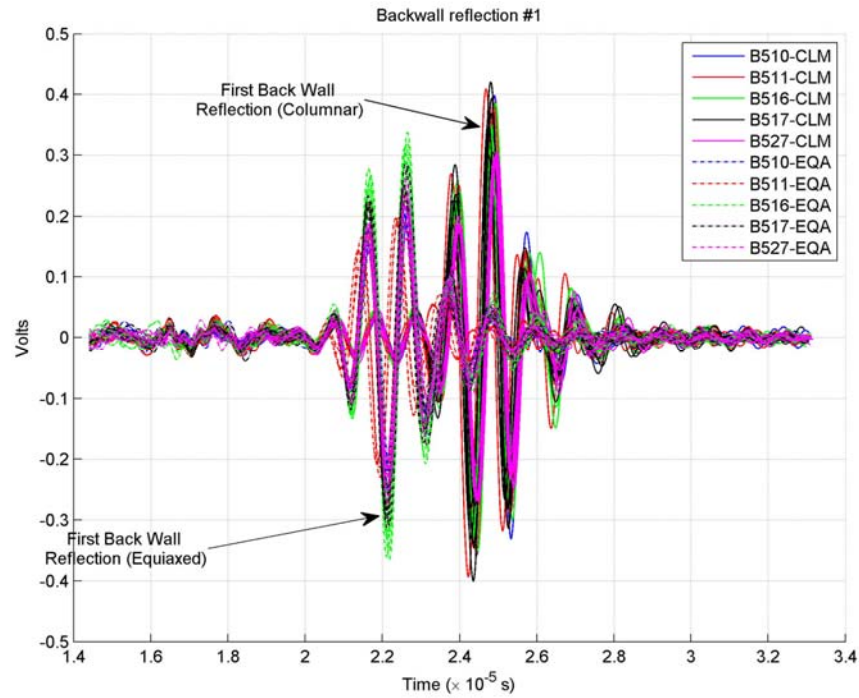
Figure 3.13. First Back-Wall Reflection Signal, after Time Gating. The figure shows all the gated signals, from all specimens.
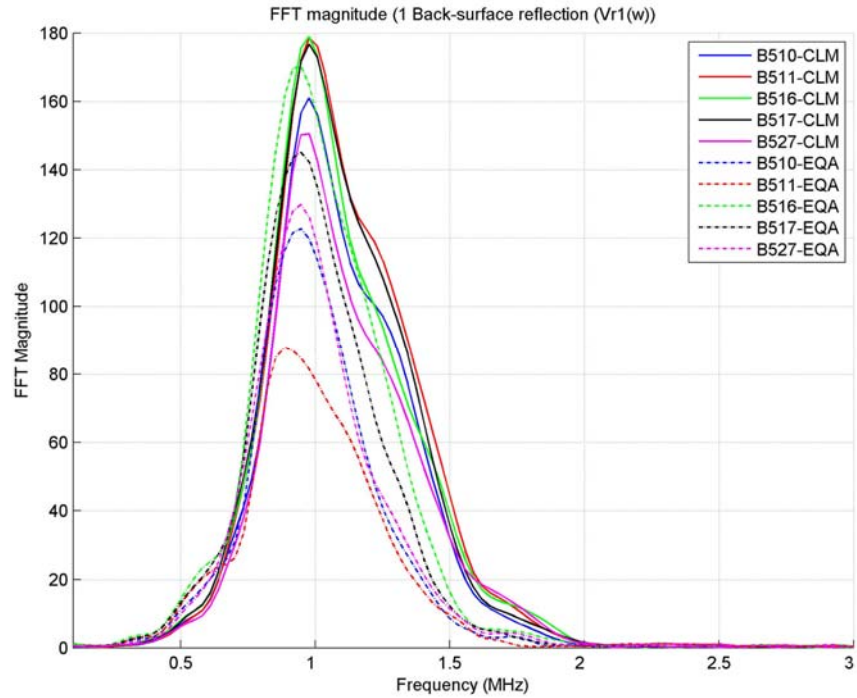
Figure 3.14. The (FFT) Magnitude Spectrum for the First Back-Wall Signal. All signals from a single region on the same specimen were averaged. A Hamming window was applied to the averaged signal before the FFT was computed.
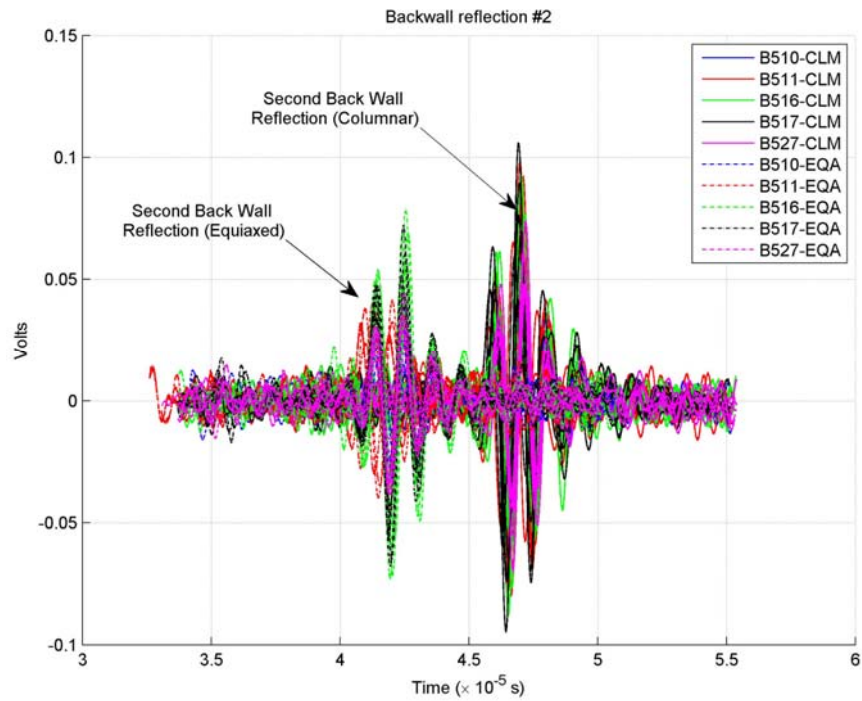
Figure 3.15. Second Back-Wall Reflection Signal, after Time Gating. The figure shows all the gated signals, from all specimens.

27
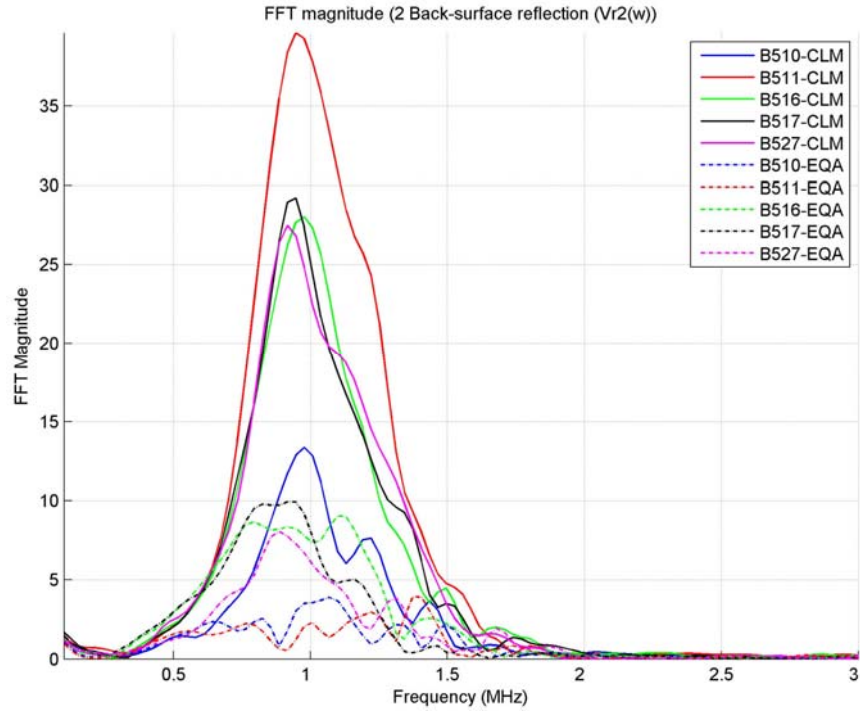
Figure 3.16. The (FFT) Magnitude Spectrum for the Second Back-Wall Signal. All signals from a single region on the same specimen were averaged. A Hamming window was applied to the averaged signal before the FFT was computed.
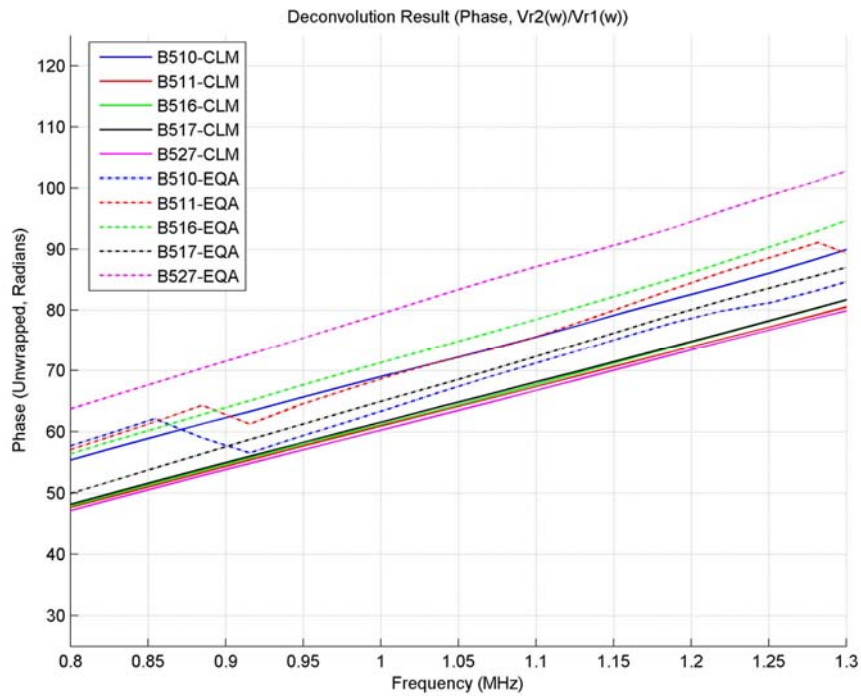
Figure 3.17. The (Unwrapped) Phase (in radians) of the Transfer Function that Results from the Deconvolution Procedure in Step 5.

28
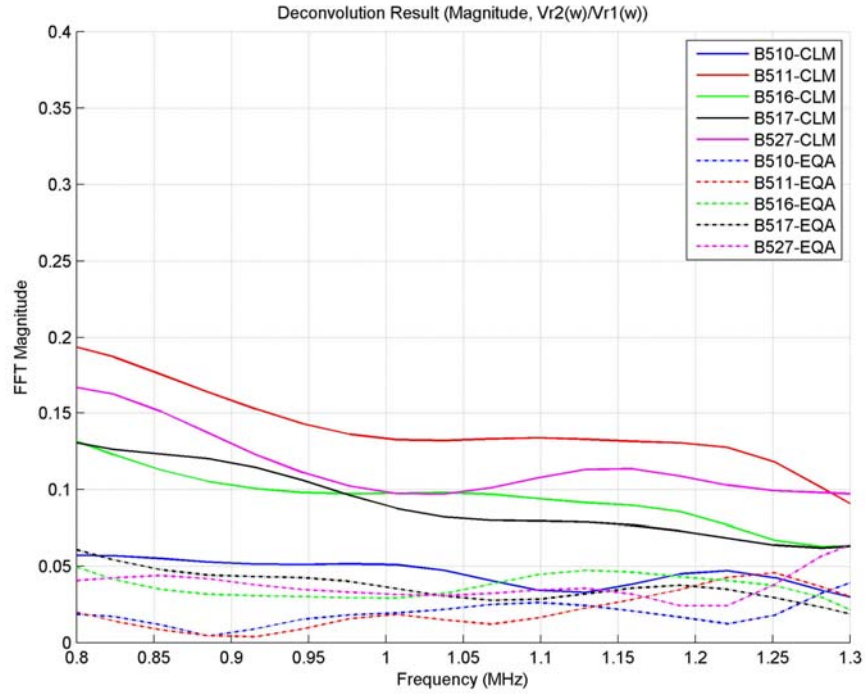
Figure 3.18. The Magnitude of the Transfer Function ($t_A(\omega)$) that Results from the Deconvolution Procedure in Step 5.
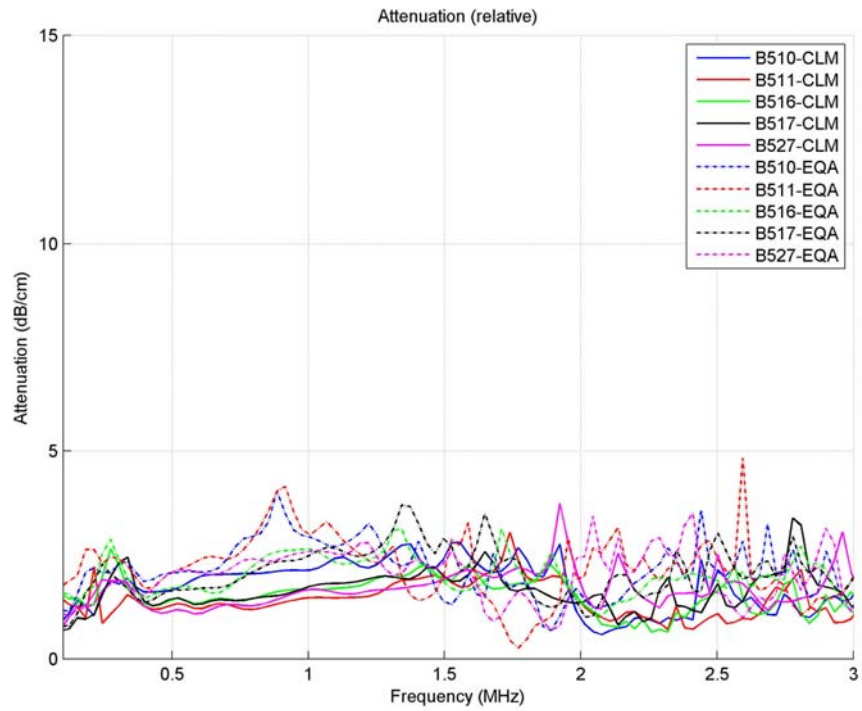
Figure 3.19. The Calculated Attenuation for Each of the 10 Regions (5 columnar and 5 equiaxed) as a Function of Frequency
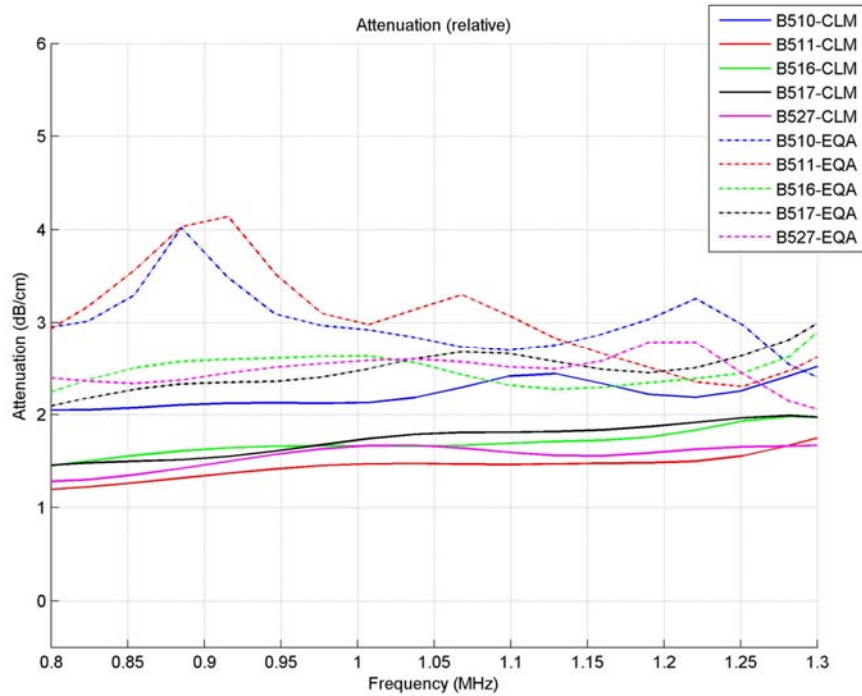
Figure 3.20. A Close-Up View of the Attenuation Between 800 kHz and 1.3 MHz

3.4.5   Longitudinal Wave Attenuation Results at 500 kHz

The attenuation calculations were also repeated using data from the 500-kHz transducer. The data was analyzed using the same procedure outlined above for the 1 MHz data. An examination of the time-domain measurements indicated that the attenuation coefficient appeared to be different when comparing the first and second back-wall reflections, and the second and third back-wall reflections (Figure 3.21). Therefore, the attenuation was computed using the first and second back-wall reflections (Figure 3.22), as well as using the second and third back-wall reflections (Figure 3.23). Examination of the region corresponding to the approximate bandwidth of the transducer shows no difference in attenuation between columnar and equiaxed regions, when using the first and second reflections Figure 3.22. However, small differences in the attenuation are apparent when using the second and third reflections (Figure 3.23). It is likely that at these lower frequencies (longer wavelengths) scattering from the grain boundaries (whether equiaxed or columnar) is low, particularly for small ultrasonic path lengths (corresponding to the first back-wall signal). As the path length increases (corresponding to second, third, and later reflections), scattering from the more numerous grain boundaries in equiaxed structures becomes more significant and results in larger attenuation values.

3.4.6   Discussion

Estimates of longitudinal wave attenuation appear to have the potential to classify CASS material as equiaxed-grain or columnar-grain material. Data showed moderate scatter; however, equiaxed-grain material exhibited more attenuation than columnar-grain material over the bandwidth of the transducers. However, it was observed that the difference in attenuation was smaller, at lower frequencies (300 kHz to

800 kHz). The trend of lower/higher attenuation for columnar/equiaxed-grain material was as predicted by Ahmed and Thompson (1995). The data in Figure 3.20 and Figure 3.23 may be used to compute the average attenuation over all columnar and equiaxed specimens at a specific frequency. The results are shown in Table 3.1. These indicate that attenuation less than ~2 dB/cm denoted columnar-grain material while a value greater than or equal to ~2.5 dB/cm denoted equiaxed-grain material.

Table 3.1. Average Attenuation Estimates in Columnar and Equiaxed Specimens at 500 kHz and 1 MHz. The statistics are based on five columnar specimens and five equiaxed specimens.

| Frequency | Columnar Microstructure | | Equiaxed Microstructure | | Figure with Relevant Data |
	Mean Attenuation (dB/cm)	Standard Deviation (dB/cm)	Mean Attenuation (dB/cm)	Standard Deviation (dB/cm)	
500 kHz	1.92	0.17	2.64	0.20	3.23
1 MHz	1.74	0.24	2.72	0.21	3.20

When examining data from the same transducer (1 MHz), a small downward shift (on the order of 10–20 kHz or lower) in the peak frequencies between consecutive back-wall reflections was observed for some of the specimens. This observation may be explained by the slightly higher attenuation values at higher frequencies (the upward trend in Figure 3.19). (Note the flatter attenuation curve in the data from the 500-kHz transducer; no significant changes in the peak frequency were observed for this data.) However, the shift was not consistent enough (or observed in all specimens that were examined) to be used to discriminate between the two grain structures. Further experiments are needed to determine if the frequency shift is consistently observed in CASS specimens (possibly using higher sampling rates, broadband transducers or higher frequency transducers). Furthermore, the value of attenuation computed using the lower frequency data (500-kHz transducer) is on the same order of magnitude as that computed at higher frequencies (1-MHz transducer). This may be due to the qualitative nature of the calculation, or it may represent a baseline attenuation value for these materials; additional studies are needed to resolve this question. Note that an effect not accounted for in our hypothesis was the acoustic lens effect caused by beam skew that occurs for columnar-grain material, and which may affect the attenuation and frequency shift. Further, attenuation in equiaxed-grain materials depends on the texture and related degree of anisotropy (Papadakis 1965; Hudgell and Gray 1985). The metallographic characterization of specimen B515 indicates a preferred direction for the dendritic colonies in the equiaxed region. While this may not be representative of the other specimens, such preferred orientation will impact scattering, attenuation and velocity measurements, and is not accounted for in our hypothesis.

(a)

(b)
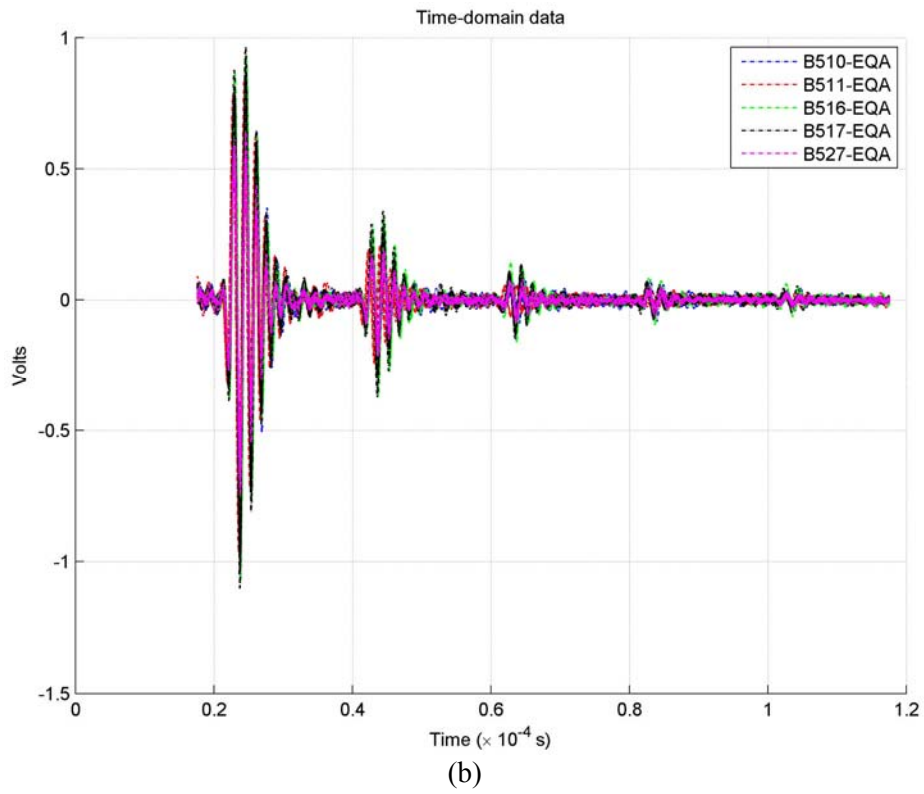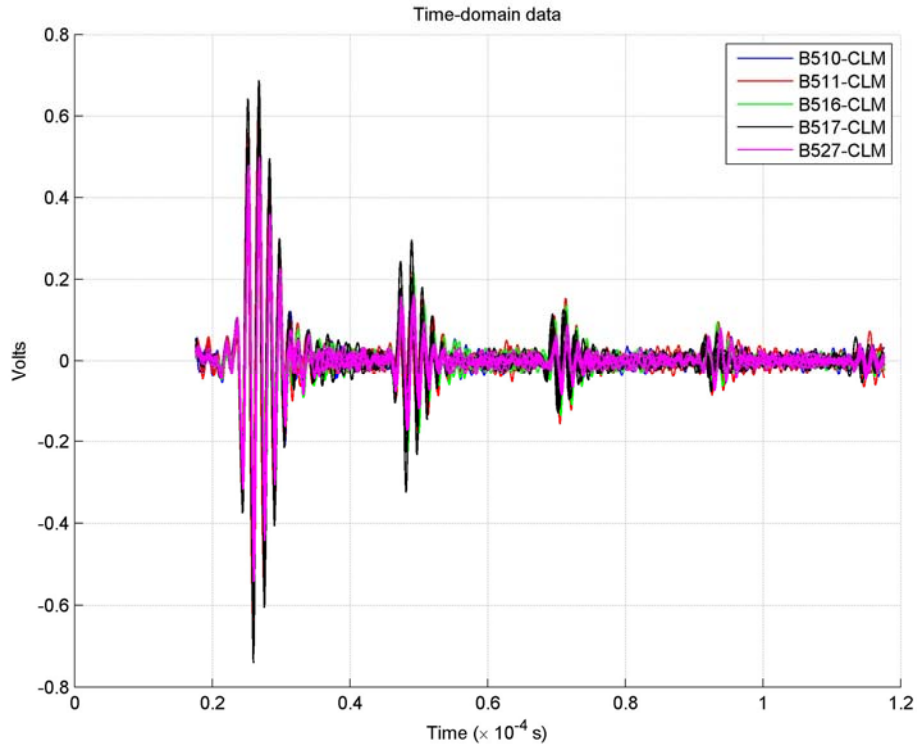
Figure 3.21. Time Domain Signals Using a 500-kHz Transducer: (a) Columnar (b) Equiaxed

(a)

(b)
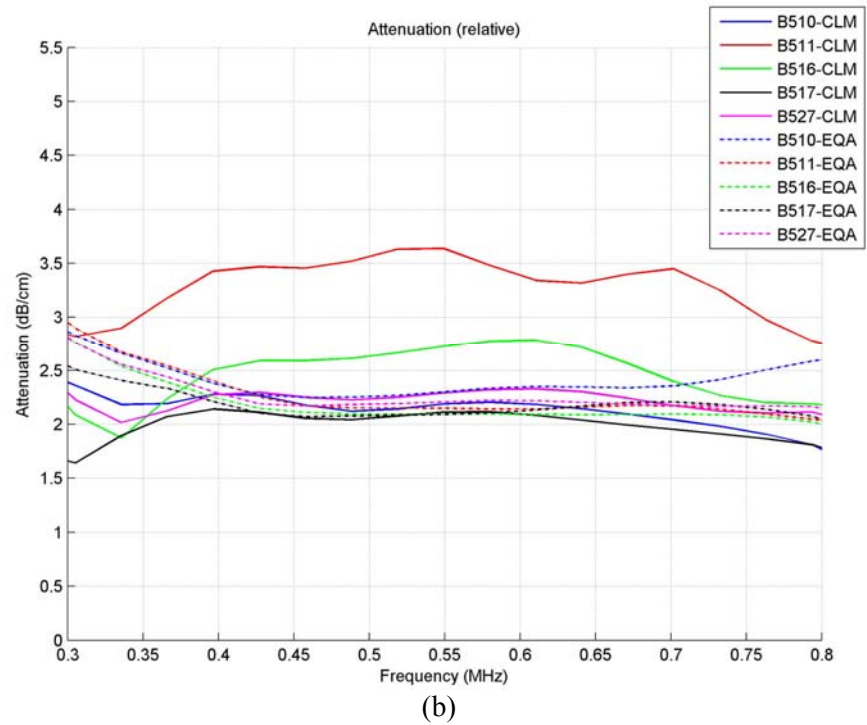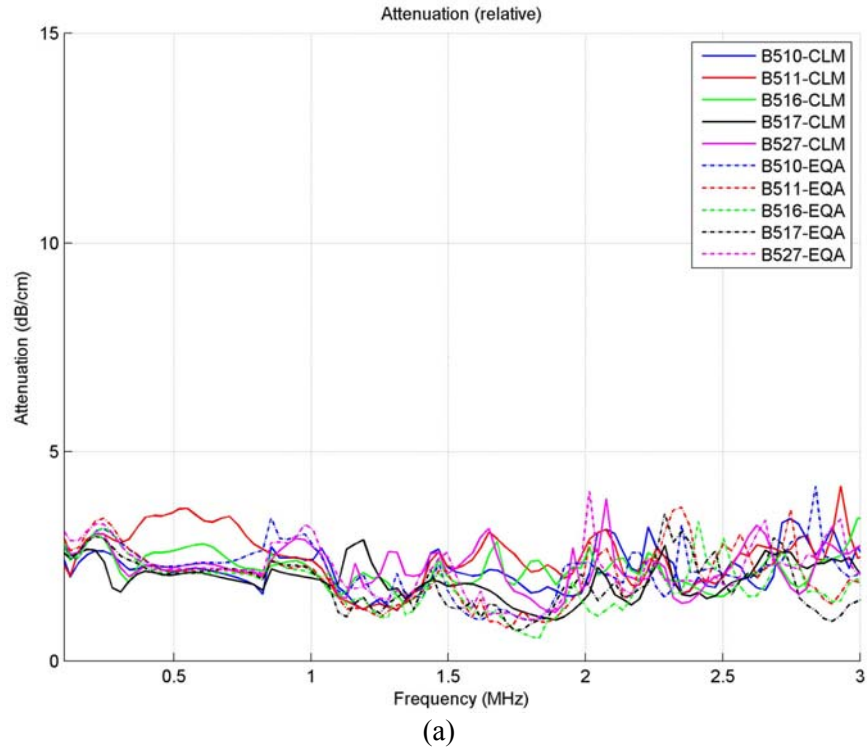
Figure 3.22. Attenuation Calculations Using a 500-kHz Transducer, and the First and Second Back-Wall Reflections: (a) 100 kHz–3 MHz, (b) 300 kHz–800 kHz (approximate bandwidth of the transducer)
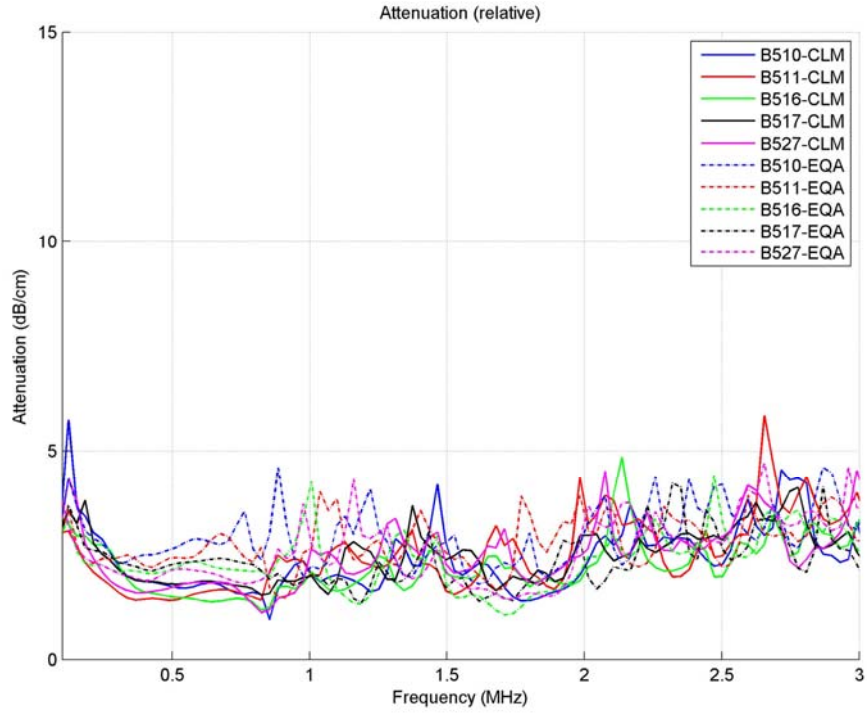
(a)
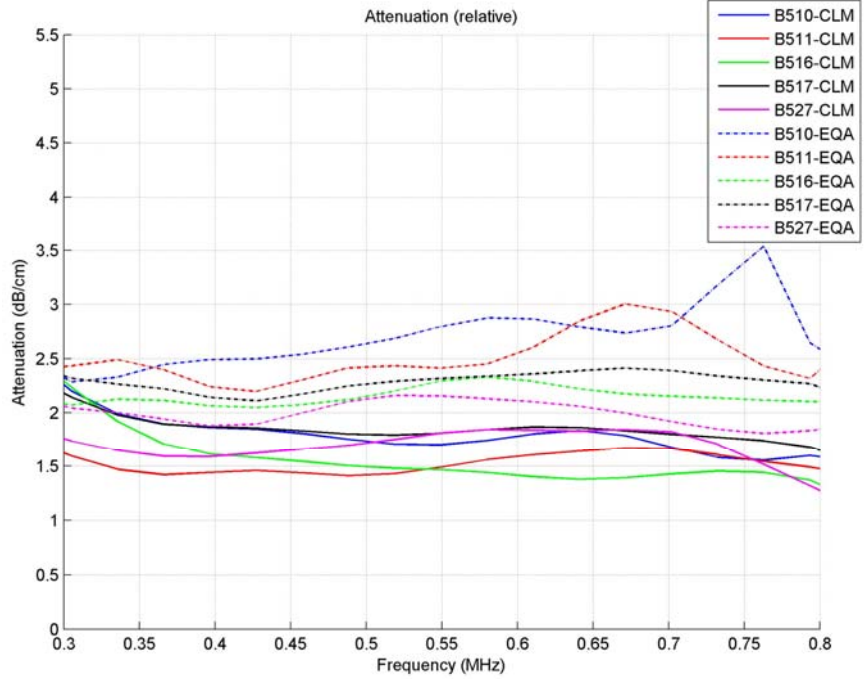
(b)

Figure 3.23. Attenuation Calculations Using a 500-kHz Transducer and the Second and Third Back-Wall Reflections: (a) 100 kHz–3 MHz, (b) 300 kHz–800 kHz (approximate bandwidth of the transducer)

An examination of the individual RF signals recorded in this experiment indicated that the signal characteristics (and the attenuation) vary somewhat from one location to another on the same specimen. This may be a result of varying grain structure over the region of the specimen, and the phenomenon requires further study.

The attenuation estimates calculated above must be used with caution. Several variables used in the calculations are not known precisely (particularly the phase velocity used in the calculation of the diffraction correction term). Additionally, the true thickness of the specimen will not be known in practice, resulting in only a qualitative estimate of the attenuation. Some experimental variables such as the ultrasonic coupling must also be controlled carefully to obtain reliable estimates of the attenuation. Finally, while the procedure described above results in the absolute value of attenuation, what may be more useful is the relative attenuation (columnar relative to equiaxed, or attenuation relative to reference samples) to enable in-situ classification of grain structure.

4.0   Conclusions and Recommendations

This document summarizes a proof-of-concept study of in-situ ultrasonic methods for classification and/or characterization of material microstructures in CASS components from the outside surface of a pipe. The results demonstrated the potential of ultrasonic measurements to classify the material type of cast austenitic stainless steel (CASS) for two consistent microstructures. Given the simple two-class problem of material being either equiaxed-grain material or a columnar-grain material, two ultrasonic parameters performed well. The time-of-flight ratio of normal incidence shear waves to normal incidence longitudinal waves (TOFRSL) and longitudinal wave attenuation appear to provide a reliable means to correctly classify material type. Qualitative TOFRSL estimates and a threshold algorithm classified all 10 material samples correctly and indicated a potentially reliable and robust technique. Qualitative longitudinal wave attenuation estimates and a threshold algorithm also classified all 10 samples correctly; however, at least in this initial study, the technique was not as robust as TOFRSL. The experiments provided promising results and demonstrated that there is a good basis to believe that potential exists for further development of these techniques for real-time classification of CASS material.

A disadvantage of the two parameters studied in this report is that both parameters are an average over thickness; therefore, a characterization as a function of time or depth is difficult. Acoustic backscatter can potentially characterize localized material volumes as a function of depth when a temporal gate is used; however, this experiment was not performed because it was not selected as a goal for this initial assessment of material characterization.

In developing this investigation into potential ultrasonic classification techniques of microstructure using in-situ measurements on CASS, work will focus on refining TOFRSL and acoustic attenuation measurement protocols, conducting proof-of-concept experiments for acoustic backscatter as a function of incident angle, and other techniques that can be used to characterize inhomogeneous and anisotropic material. Continuing work includes:

- Verifying repeatability of the experiments, and confirming the results using additional specimens that are representative of the columnar and equiaxed grain structure (as well as mixed grain structures). The microstructures selected should seek to be representative of the majority of microstructures that can be encountered in current legacy U.S. nuclear power plant components.

- Enhancing TOFRSL estimates by investigating more effective coupling, including potential use of electromagnetic acoustic transducers (EMATs) to transmit and receive normal incidence shear waves (EPRI 1991), and moving toward a quantitative estimate by use of arrival time calibration and compensation for diffraction.

- Enhancing acoustic attenuation estimates by investigating more effective coupling, use of EMATs, and shear-wave attenuation measurements, computing attenuation estimates over a broader frequency range through the use of broadband transducers employing swept frequency excitation.

- Evaluating the use of a delay line for time-of-flight and attenuation measurements. The delay line may be contoured to match the curvature of the specimen at one end, and the profile of the transducer face at the other. This will better control any problems with inadequate coupling. Further, the use of a delay line minimizes any potential problems with near-field data and separates out the different back-surface signals in time. The use of a delay line also has an added advantage in the form of an

available front-surface reflection that may be used for robust estimation of attenuation (Papadakis 1968), even when a second back-wall reflection is unavailable.

- Conducting backscatter measurements for improved depth resolution in classifying CASS microstructure with known through-wall variability.

- Evaluating other ultrasonic or electromagnetic methods used for microstructure and material characterization in other applications, that can be leveraged and applied to the CASS microstructural characterization challenge.

- Assessing the applicability of these techniques to characterizing cast primary circuit components (safe ends, elbows, or pipes) through inspection from the ID surface. According to ASME Code requirements, inspections from the ID need only inspect the inner 1/3 of the wall. The techniques evaluated in this report provide microstructure information averaged over the entire wall thickness. The use of backscatter measurements may provide better depth resolution, and microstructure characterization in the required volume.

5.0   References

Ahmed S and RB Thompson. 1995. "Influence of Columnar Microstructure on Ultrasonic Backscattering." In *Review of Progress in Quantitative Nondestructive Evaluation (QNDE)*, Vol. 14, pp. 1617–1624. eds: DO Thompson and DE Chimenti. Plenum Press, New York.

Anderson MT, SL Crawford, SE Cumblidge, KM Denslow, AA Diaz and SR Doctor. 2007. *Assessment of Crack Detection in Heavy-Walled Cast Stainless Steel Piping Welds Using Advanced Low-Frequency Ultrasonic Methods*. NUREG/CR-6933, PNNL-16292, U.S. Nuclear Regulatory Commission, Washington, D.C.

Auld BA. 1973. *Acoustic Fields and Waves in Solids, Volume 1*. John Wiley & Sons, New York.

Bencharit U, JL Kaufman, NM Bilgutay and J Saniie. 1986. "Frequency and Spatial Compounding Techniques for Improved Ultrasonic Imaging." In *IEEE 1986 Ultrasonics Symposium*, pp. 1021–1026. November 17–19, 1986, Williamsburg, Virginia. IEEE, New York.

Bilgutay NM, U Bencharit and J Saniie. 1989. "Enhanced Ultrasonic Imaging with Split Spectrum Processing and Polarity Thresholding." *IEEE Transactions on Acoustics, Speech and Signal Processing* 37(10):1590–1592.

Bordier JM, M Fink, A Le Brun and F Cohen-Tenoudji. 1991. "The Influence of Multiple Scattering in Incoherent Inspection of Coarse Grain Stainless Steel." In *Proceedings of the 1991 IEEE Ultrasonics Symposium*, pp. 803–808. December 8–11, 1991, Orlando, Florida. DOI 10.1109/ULTSYM.1991.234079. IEEE, New York.

Chen J, Y Shi and S Shi. 1999. "Noise Analysis of Digital Ultrasonic Nondestructive Evaluation System." *International Journal of Pressure Vessels and Piping* 76(9):619–630.

Choi MH. 2007. "Spatial Compounding from Ultrasonic RF Data for Speckle Reduction in Ultrasonic Diagnostic Imaging System." In *International Conference on Control, Automation and Systems, ICCAS 2007*, pp. 1577–1580. October 17–20, 2007, Seoul, Korea. IEEE Computer Society, Piscataway, New Jersey. http://dx.doi.org/10.1109/ICCAS.2007.4406591.

Cumberland J. 1963. "Centrifugal Casting Techniques." *The British Foundryman* January:26–47.

Diaz AA, SR Doctor, BP Hildebrand, FA Simonen, GJ Schuster, ES Andersen, GP McDonald and RD Hasse. 1998. *Evaluation of Ultrasonic Inspection Techniques for Coarse-Grained Materials*. NUREG/CR-6594, PNNL-11171, U.S. Nuclear Regulatory Commission, Washington, D.C.

EPRI. 1991. *Application of Electromagnetic Acoustic Transducers to Coarse-Grained Material*. EPRI NP-7438, Electric Power Research Institute, Palo Alto, California.

EPRI. 2005. *Assessment of Cast Stainless Steel Inspection*. Report 101160, Electric Power Research Institute, Palo Alta, California.

Ericsson L. 1994. *Reduction of Material Noise in Ultrasonic Nondestructive Evaluation Using Synthetic Frequency Diversity Algorithms*. Thesis, Teknikum Institute of Technology, Uppsala University, Uppsala, Sweden. ISSN 0346-8887.

Ghoshal G and JA Turner. 2009. "Diffuse Ultrasonic Backscatter in a Two-Dimensional Domain." *Acta Mechanica* 205(1–4):35–49.

Ghouti L. 1997. "High-Order Spectra-Based Deconvolution of Ultrasonic NDT Signals for Defect Identification." *Ultrasonics* 35(l7):525–531.

Goebbels K. 1980. "Chapter 4, Structure Analysis by Scattered Ultrasonic Radiation." In *Research Techniques in Nondestructive Testing, Vol. IV*. ed: RS Sharpe. Academic Press, Inc., New York.

Goebbels K. 1994. *Materials Characterization for Process Control and Product Conformity*. CRC Press, Boca Raton, Florida.

Gonzalez RC and RE Woods. 1999. *Digital Image Processing*. Addison-Wesley, Reading, Massachusetts.

Good MS, BP Hildebrand and CM Batson. 1991. "Phase Mapping of Ultrasonic Fields Passed Through Centrifugally Cast Stainless Steel." In *Review of Progress in Quantitative Nondestructive Evaluation (QNDE)*, Vol. 10B, pp. 1975–1982. July 15–20, 1990, La Jolla, California. Plenum Press, New York.

Hargreaves ML. 1988. *Digital Processing of Ultrasound Signals Back-scattered from Coarse Grained Austenitic Stainless Steel*. Ph.D. Thesis, University of Keele, Keele, Staffordshire, England.

Haykin S. 1991. *Adaptive Filter Theory, 2nd Edition*. Prentice-Hall, Englewood Cliffs, New Jersey.

Hildebrand BP, MS Good, AA Diaz and ER Green. 1992. "Application of Critical Angle Imaging to the Characterization of Cast Stainless Steels." *Review of Progress in Quantitative Nondestructive Evaluation* 11A:863–870.

Hudgell RJ and BS Gray. 1985. *The Ultrasonic Inspection of Austenitic Materials – State of the Art Report*. ND-R-1201(R); CSNI Report No. 94, United Kingdom Atomic Energy Authority, Risley Nuclear Power Development Establishment, Risley, Warrington, United Kingdom.

Jenson F, T Fortuna and L Doudet. 2009. "Modeling of Ultrasonic Propagation in a Coarse Grain Structure." In *Proceedings of the 35th Annual Review of Progress in Quantitative Nondestructive Evaluation*, pp. 1201–1208. July 20–25, 2008, Chicago, Illinois. American Institute of Physics, Melville, New York.

Jeong P and F Ammirato. 1989. "Ultrasonic Material Characterization of Cast Stainless Steel." In *12th World Conference on NDT*, pp. 199–203 Amsterdam.

Jeong YH. 1987. *An Ultrasonic Material State Classifier for Elastically Anisotropic Materials*. Ph.D. Thesis, Drexel University, Philadelphia, Pennsylvania.

Kumar AS, T Jayakumar and B Raj. 2000. "Ultrasonic Spectral Analysis For Microstructural Characterization of Austenitic and Ferritic Steels." *Philosophical Magazine A* 80(11):2469–2487.

Kupperman DS, KJ Reimann and J Abrego-Lopez. 1987. "Ultrasonic NDE of Cast Stainless Steel." *NDT International* 20(3):143–206.

Kupperman DS, KJ Reimann and DI Kim. 1981. "Ultrasonic Characterization and Microstructure of Stainless Steel Weld Metal." In *Proceedings of Nondestructive Evaluation: Microstructural*

Characterization and Reliability Strategies, pp. 1990–216. October 5–9, 1980, Pittsburg, Pennsylvania. The Metallurgical Society of AIME, Warrendale, Pennsylvania.

Miralles R, L Vergara and J Gosalbez. 2004. "Material Grain Noise Analysis by Using Higher Order Statistics." *Signal Processing* 84:197–205.

Morris JB, DA Pommet, MA Fiddy and RV McGahan. 1995. "Imaging of Strongly Scattering Object Using a Nonlinear Filtering Technique." In *Proceedings of SPIE - The International Society for Optical Engineering*, Vol. 2570, pp. 27–37. July 10–11, 1995, San Diego, California. Society of Photo-Optical Instrumentation Engineers, Bellingham, Washington.

Nageswaran CRB and A Whittle. 2008. "Immersion Transmit-Receive Longitudinal Phased Array Probe for Stainless Steel." *Insight* 50(12):673–678.

Newhouse VL, P Karpur, JL Rose and I Amir. 1985. "A New Technique for Clutter Reduction in Ultrasonic Imaging." In *Proceedings of IEEE 1985 Ultrasonics Symposium*, Vol. 2, pp. 998–1003. October 16–18, 1985, San Francisco, California. IEEE, New York.

Northcott L and V Dickin. 1944. "The Influence of Centrifugal Casting (Horizontal Axis) Upon the Structure and Properties of Metals." *The Journal of the Institute of Metals* LXX:301–323.

Northcott L and D McLean. 1945. "The Influence of Centrifugal Casting Upon the Structure and Properties of Steel." *The Journal of the Iron and Steel Institute* CLI:303–328.

Papadakis EP. 1965. "Influence of Preferred Orientation on Ultrasonic Grain Scattering." *Journal of Applied Physics* 36(5):1738–1740.

Papadakis EP. 1968. "Buffer-Rod System for Ultrasonic Attenuation Measurements." *Journal of the Acoustical Society of America* 44(5):1437–1441.

Park SC, YS Lee and SJ Kim. 2004. "Threshold Varying Method of Stationary Wavelet Denoising for Ultrasonic Speckle Reduction." *Materials Science Forum* 449–452:1153–1156.

Schmer LW and S-J Song. 2007. *Ultrasonic Nondestructive Evaluation Systems – Models and Measurements*. Springer, New York.

Shankar PM, P Karpur, VL Newhouse and JL Rose. 1989. "Split-Spectrum Processing: Analysis of Polarity Thresholding Algorithm for Improvement of Signal-to-Noise Ratio and Detectability in Ultrasonic Signals." *IEEE Transactions on Ultrasonics, Ferroelectrics, and Frequency Control* 36(1):101–108.

Silverstein SD and LJ Thomas. 1993. "Analytical Comparison of Sensor Signal Processing Enhancements for NDT Synthetic Aperture Ultrasonic Imaging." *IEEE Transactions on Image Processing* 2(1):60–67.

Steele JH and JL McCall. 1984. *STP839, Practical Applications of Quantitative Metallography*. ASTM International, West Conshohocken, Pennsylvania.

Thompson RB, FJ Margetan, P Haldipur, L Yu, A Li, P Panetta and H Wasan. 2008. "Scattering of Elastic Waves in Simple and Complex Polycrystals." *Wave Motion* 45:655–674.

Appendix A

Characterization of Cast Stainless Steel Piping

Appendix A

Characterization of Cast Stainless Steel Piping

Dan Edwards
Alan Schemer-Kohrn
Clyde Chamberlin

December 2008

A.1 Statement of Work

The texture and microstructure of a large piece of cast stainless steel piping was characterized using scanning electron microscopy (SEM) and electron backscatter diffraction (EBSD) analysis. The pipe sample is labeled as axial-radial cross section of PNNL Specimen B515. The purpose was to understand the microstructural variations through the pipe wall from two regions on either side of a weld joint in the pipe. The piping was welded together from two different cast stainless steel conditions, both of which were assumed to be centrifugally cast. The grain structure and overall texture were explored using EBSD, a technique which directly measures the orientation at any point within a grain that is excited by the electron beam (100–300 nm diameter probe) in the scanning electron microscope. Because the beam is scanned over the area of interest with high precision, orientation maps can be generated to measure the orientations of any phase(s) present with respect to any predetermined specimen axis. By virtue of the crystallographic information derived from the measurements, direct measurements of the phase distributions can also be derived depending on the size and volume fraction of each phase. This information can also be directly correlated with the chemistry of each phase. EBSD can also provide qualitative estimates of residual strains within the sample by measuring the density of misorientation boundaries within a region of interest and information about the types of grain boundaries and other interfaces within the examined area. For this task, the initial effort was limited to measuring the overall texture of the austenite phase on each side of the weld joint.

A.2 Experimental Conditions

Figure A.1a shows a montage of optical images of the section of the B515 cast stainless steel piping given a mild mechanical polish and acid etched to reveal the gross grain structure. A close-up of the weld region joining the two halves of the tubes is shown in Figure A.1b. This latter image, provided to us by Morris Good, was taken from a section of the same piping, but given a higher quality mechanical polish and acid etched to better reveal the grain structure. The left side of the sample is characterized by very large, millimeter size columnar grains oriented perpendicular to the pipe outer surface, whereas the right side of the weld has an apparent equiaxed grain structure that cannot be distinguished easily at these magnifications in the optical image. A piece from each end of the piping sample was removed by cutoff saw from approximately 20 cm from the weld centerline and sub-divided into 3 separate pieces as shown in Figure A.1a. Each piece was then mounted in epoxy and mechanically polished down to a 0.05 µm
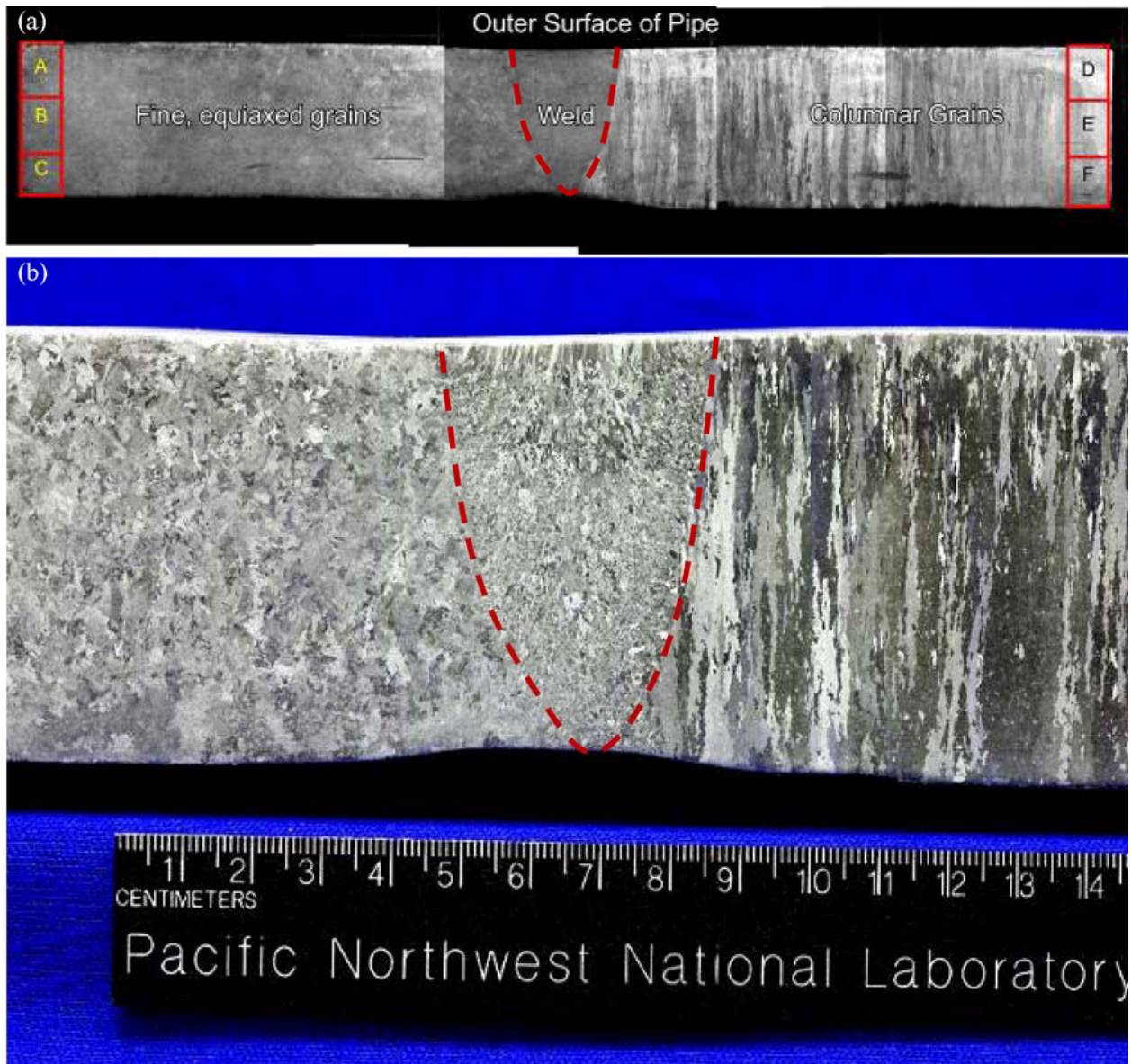
Figure A.1. A Composite Image is Provided in (a) Showing the Overall Width of the Piping Section Provided for EBSD Analysis. The areas selected for characterization are highlighted in red and labeled in yellow. A close-up is provided in (b) to better show the grain structure on each side of the weld zone. The view is the axial-radial cross section of PNNL Specimen B515.

colloidal silica finish. For EBSD, each specimen was mounted and loaded into the SEM in the same manner such that in the following images, the specimen normal is the axial direction, the radial direction is vertical with the pipe outer surface at the top and the transverse direction is horizontal. A schematic is provided in Figure A.2 to show the indicated axis referenced to the original pipe.
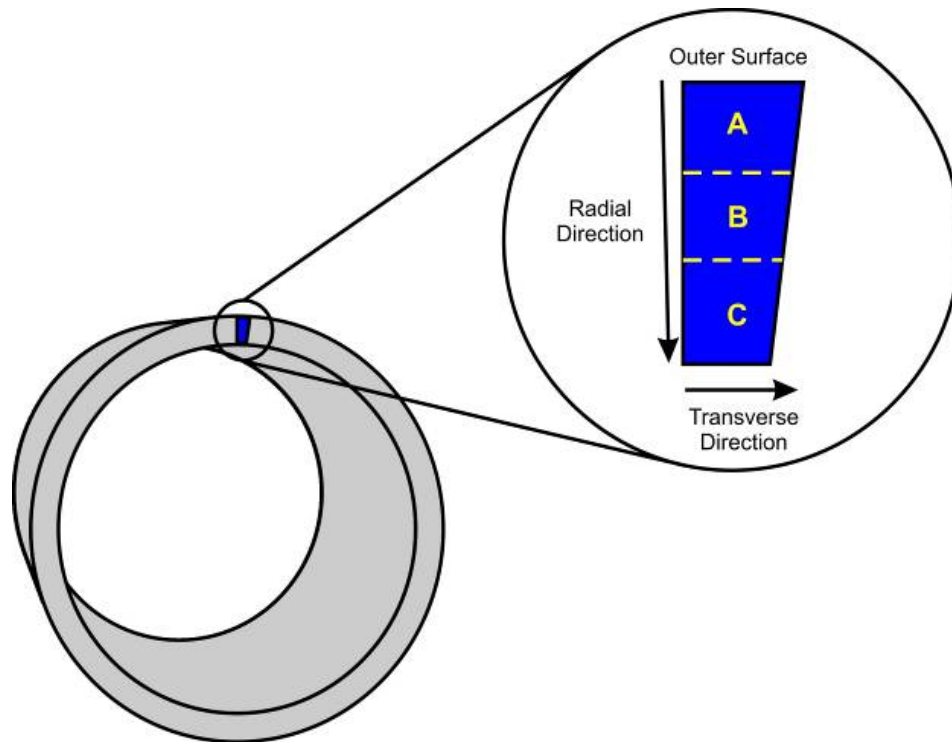
Figure A.2. Schematic Showing How the Sample from Each End of the Pipe Cross-Section was Cut and Mounted in Epoxy. The direction normal to the page is the axial direction of the pipe.

The texture and grain structure were characterized using EBSD in a JEOL 840 SEM. EBSD is a complementary technique in the SEM whereby Kikuchi diffraction patterns are acquired from the surface of the highly polished metal sample inclined at 70° to the SEM electron beam. The probe diameter used for this analysis was on the order of 250–300 nm, but elongated in the x-direction because of the tilt of the sample. The interaction volume of the backscattered electrons that produce the diffraction patterns is ~10–20 nm. Because of the shallow depth and sensitivity of the diffraction patterns to mechanical strain, the surface of the metallic sample has to be as deformation-free as possible. In this case, the surface is polished down to a final 0.05 μm colloidal silica finish, which produces exceptional surfaces for EBSD in stainless steels. Electropolishing and ion milling are two other approaches that can produce the requisite high quality samples. The JEOL 840 SEM is equipped with a high speed Nordlys CCD camera interfaced with the HKL software package Channel 5. The electron beam is scanned across the region of interest at a predetermined step spacing and individual diffraction patterns acquired at each step position (called pixels from this point forward). Indexing each diffraction pattern provides both the crystal phase and crystal orientation at each pixel position, effectively mapping out the orientation and phase relationships for the region of interest. The Channel 5 software allows the resulting data to be processed to reveal the grain size, types of boundaries, degree of crystal misorientation between individual pixels, and changes in any phases if present. In this study the phases were limited to austenitic stainless steel only, however, it was noted that a small volume fraction of ferrite was present in both regions of the piping. Given the low volume fraction, the EBSD work focused on the overall crystal orientation of the austenite phase.

Characterization focused primarily on the orientation mapping with limited imaging done in the SEM. The results are provided both as maps showing the orientation of individual grains as well as pole figures

that show the overall orientation distribution of the grains in the areas analyzed. A few images taken in backscatter electron imaging mode are shown just to visually highlight the differences in microstructure on each side of the weld joint. Because of the large size of the pipe cross-section, only a fraction of the area was characterized in each of the six subpieces. Each individual piece was mapped at a pixel spacing of 10 μm to produce a map of 400×400 pixels, with a total of 5–6 overlapping maps needing to be stitched together to form a complete cross-section of each individual piece. Acquisition speeds were typically 22 milliseconds per pattern. To map the through-wall thickness on the columnar and fine grained dendritic sides required roughly 15–18 maps to map out the entire thickness of the pipe wall. Additional details regarding EBSD and the data presentation are provided as an appendix to this section.

A.3 Results

As the previous optical images revealed, there were substantial differences in the grain structure on the two sides of the weld joint. Figure A.3 provides a comparison of backscatter electron (BSE) images taken in the SEM. These images reveal orientation differences due to changes in grain orientation and/or strain, and more commonly will reveal compositional differences if the average atomic number difference of one phase is different than another phase. In these case of the images, there are two phases present, one a higher Ni/lower Cr austenite phase and the lower Ni/higher Cr ferrite phase. The ferrite phase is fairly low volume fraction, estimated to be less than 5%, and doesn't stand out at the magnifications used for these images and for the EBSD maps. Because of the low volume fraction, the ferrite phase was ignored during the analysis of the texture of the casting.

What is more important are the differences in overall morphology of the grains, or dendritic structure in this case, that arise because of processing differences during the casting of the two halves of the piping. The millimeter-sized elongated grains on the columnar side of the welded pipe suggest a different solidification rate than the finer-grained dendritic structure on the right-hand side of the weld joint. "Dendritic" is an expression used to describe the nucleation and growth of a solid phase from a colder mold surface into the hotter liquid stainless steel poured into the mold. A typical appearance of a dendritic structure in cast stainless steel occurs in the fine-grained region on the left-hand side of the weld joint, whereas the large columnar growth on the right-side implies little stirring and/or a slower solidification rate. However, the large columnar grains are actually multiple primary dendrites of close crystallographic orientation that can appear as a single grain, so it is in fact a "dendritic" structure, but on a different scale and more highly oriented.

In the region characterized on the columnar side, orientation mapping reveals that the large columnar grains near the surface, presumably at the chill zone where the liquid metal first came in contact with the cold mould surface, are skewed at an angle from the surface and a bit more random in their orientation. After ~10 mm, a few grains begin to dominate the microstructure at the expense of what are presumed to have been grains less favorably oriented for continued growth. According to Porter and Easterling (1983), cubic metals tend to grow preferentially in the [001] directions, so while the chill zone has a finer grain size and more random orientation of dendrites, eventually the most favorably-oriented grains win the growth competition and the microstructure changes to the observed large columnar grain structure visible in this part of the stainless steel piping. The orientation map shown in Figure A.4 reveals exactly that process, where after ~10 mm the few large grains have become dominant and for the most part are oriented with the {001} cube faces perpendicular to the growth direction (radial direction in this case). Figure A.5 shows the other inverse pole figure maps at in the z = axial and x = transverse directions,

A.4

which confirm that the dendrites in this region are highly oriented with respect to one another and the growth direction. The pattern quality image next to the color orientation maps are derived from a numerical value that relates the quality of the diffraction pattern to the measured contrast of the Kikuchi bands compared to the background. The pattern quality provides a qualitative, visual estimate of orientation differences in the sample, but is also highly sensitive to strain, either from residual scratches, from the presence of a high density of dislocations in the metal matrix, or even from stains or coatings that may not have been removed properly during the final cleaning before being placed in the SEM. The darker the region, the lower the pattern quality, however, there is yet no definitive method to separate the relative contributions from orientation effects on pattern quality versus the presence of strain the lattice, hence the PQ images are qualitative.
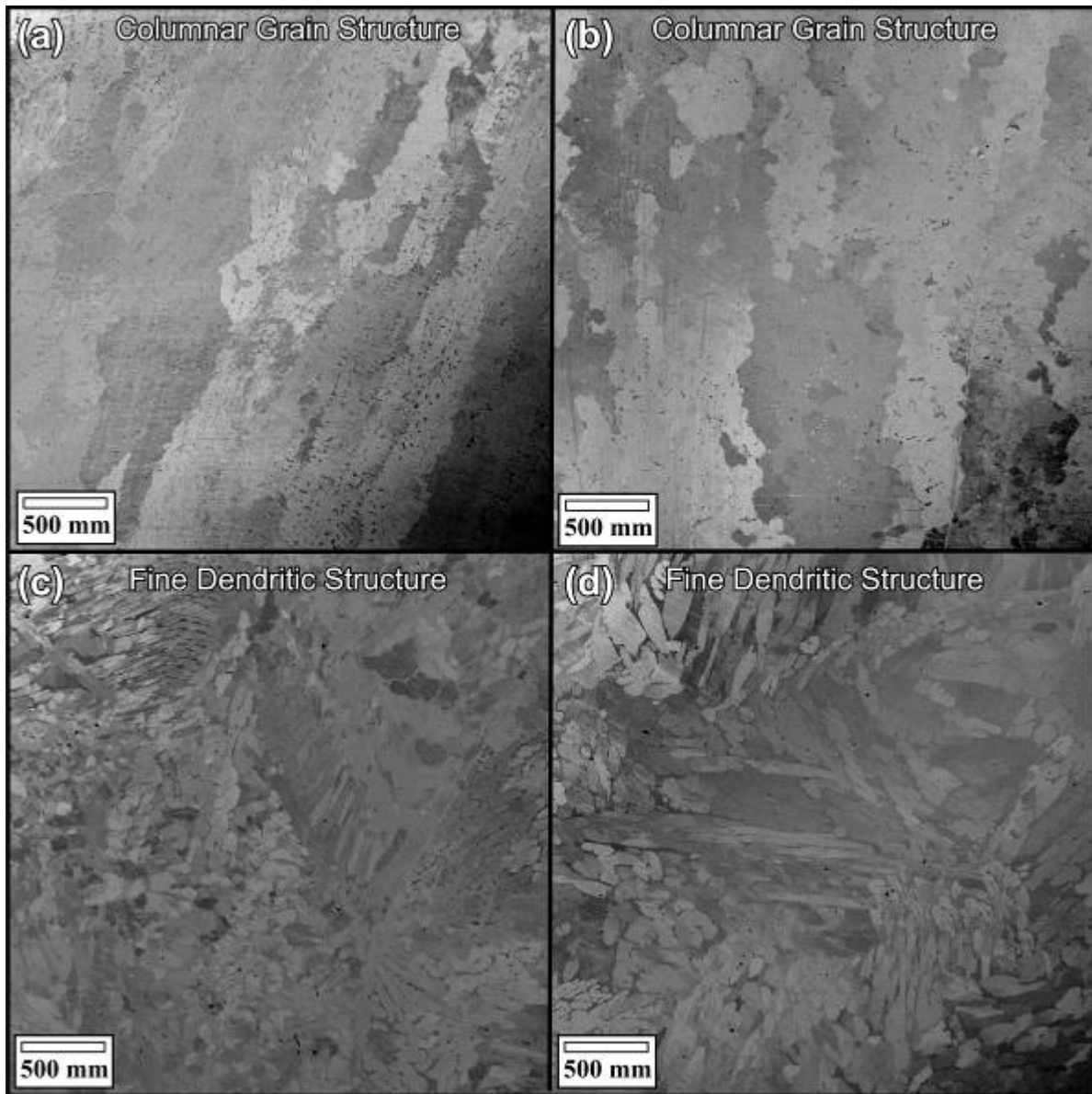
Figure A.3.   Comparison of Microstructure between the Left and Right Side of the Weld Joint as Indicated in Figure A.1.
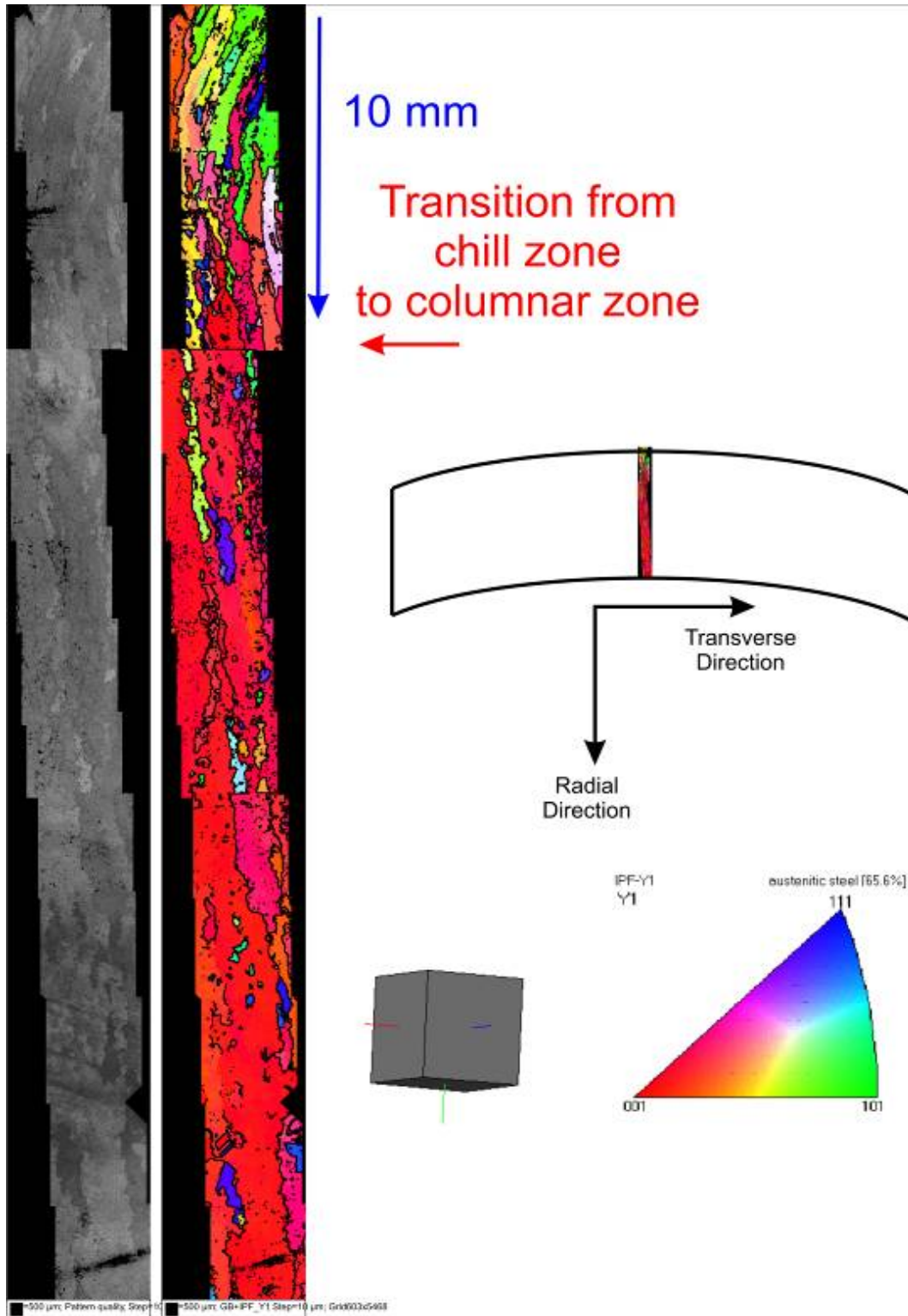
Figure A.4. Pattern Quality and Inverse Pole Figure Map Showing the Grains Colored from the Perspective of Looking Down the Y-Direction (equates to the radial direction). Red colored grains are oriented with their (001) cube faces nominally perpendicular to the growth direction.
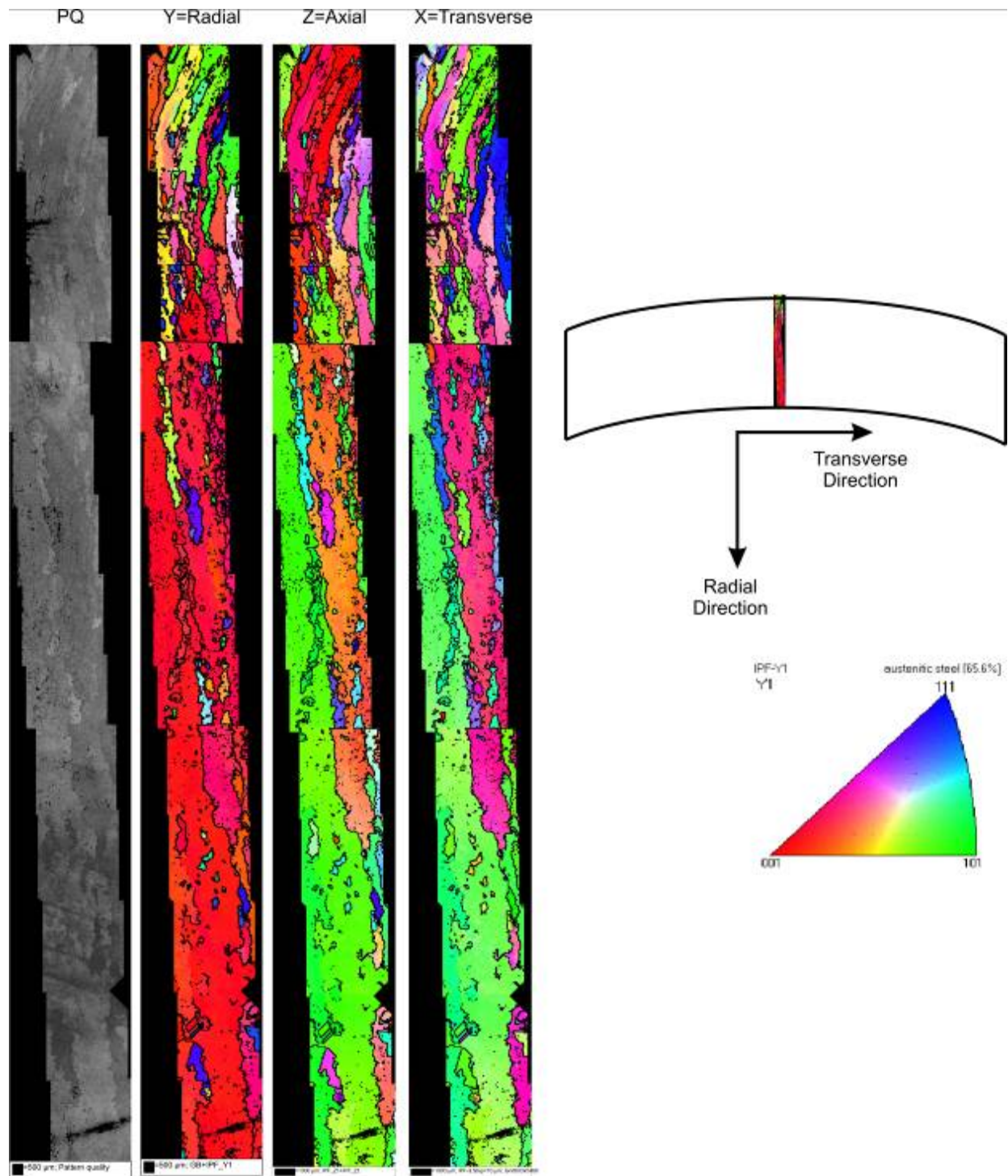
Figure A.5. A Comparison is Shown of the Pattern Quality Map and the 3 Inverse Pole Figure Maps in the y, z and x Directions. Each color maps simply shows the orientation of each region as viewed from the indicated direction. Y is the vertical direction, *Z* is normal to the page, and X is the horizontal direction.

The pole figures for the entire measured columnar region are provided in Figure A.6, confirming that the most prominent orientation is with the <001> poles aligned preferentially in the radial direction. In this particular region, the <011> poles are aligned in a secondary orientation to the Z and X-directions, that is, the axial and transverse directions of the pipe. The pole plot histograms show the absolute angular distribution of the <001> and <011> poles about the Y-direction (radial direction). In a totally random distribution there would not be any peaks in the distributions, however, in this case the presence of sharply defined peaks in the histogram is another indication of the strong preferential orientation of the dendritic structure.
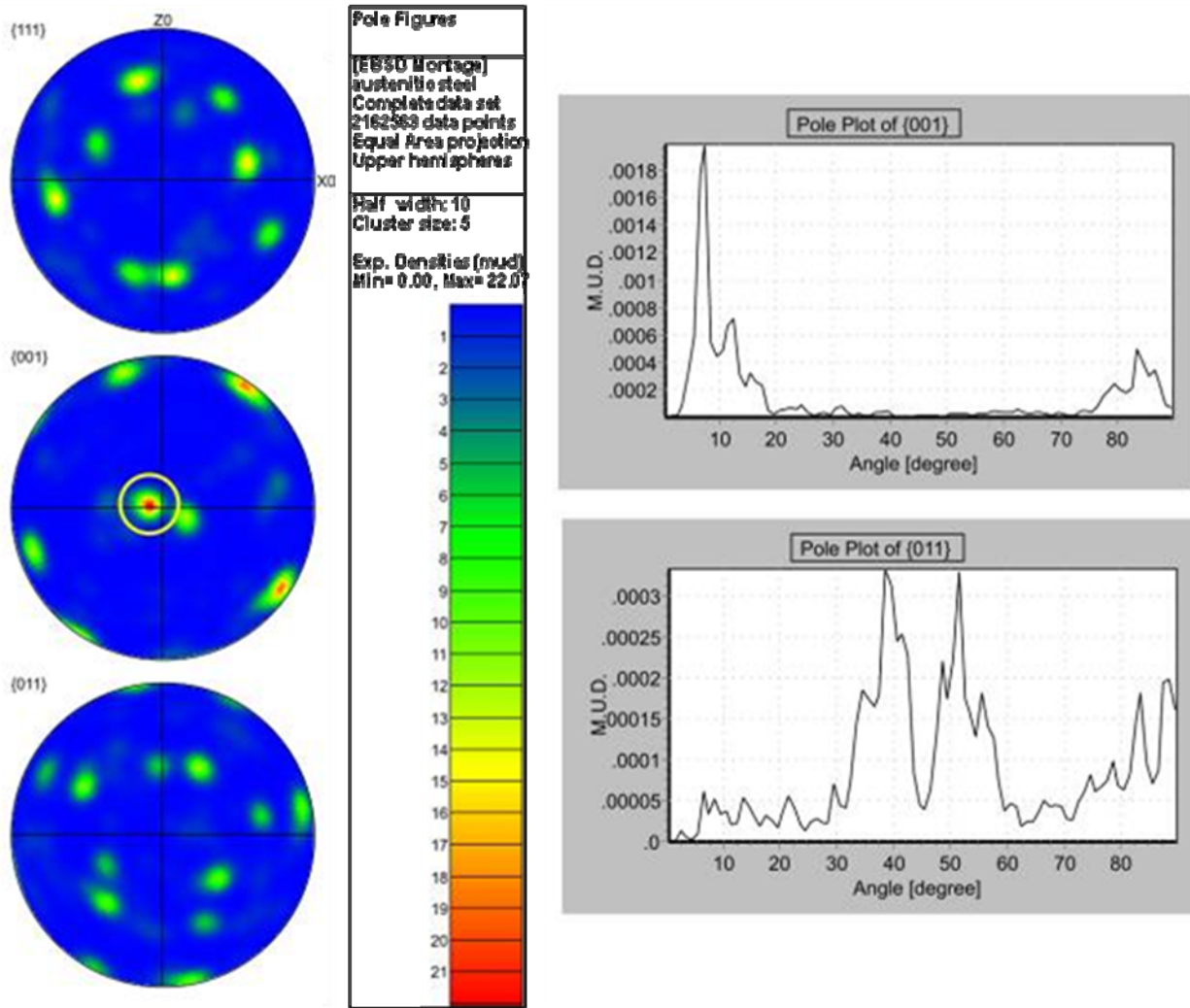
Figure A.6.   The Encircled Region on the {001} Pole Figure Shows that {001} Poles are Aligned in the Y-Direction, which Corresponds to the Radial Direction of the Pipe. A secondary orientation is present with the {011} poles are aligned with the Z and X-directions. The {001} pole plot histogram to the right indicate that peaks exist at ~8° and 85° from the radial direction, and at ~38°, 52°, 82° and 88° for the {011} poles.

In the region characterized on the fine equiaxed dendritic side of the welded pipe, the orientation maps reveal a different story. Here dendritic colonies exist that are much smaller than the highly oriented dendrites on the other side of the weld joint. A summary is provided in Figure A.7 that shows the pattern quality map and the three inverse pole figure maps for all three reference directions. The range of colors suggest that taken as a whole, this region taken as a whole doesn't have a singular orientation, but rather isolated areas related to an individual dendrite colony produce a specific localized orientation. The pole figure shown in Figure A.8 suggests a slightly different story in that over the entire region, there is some clustering of both the <001> poles and the <011> poles. In this case however, the <011> poles are more closely aligned with the Y-direction (radial direction) and the <001> poles peak at about 38° towards the axial direction. The pole plot histograms also confirm that the <011> poles are more closely clustered near the Y-direction (radial direction), whereas the histogram for the distribution of the <001> poles has peaks across the absolute angular range from the center Y-direction. The pole figures and histograms both indicate that a moderate and different preferred orientation exists in this region of the piping.

A.4 Summary and Discussion

The orientation mapping reveals that a strong orientation exists on the columnar side of the pipe, with the one set of the {001} poles aligned with the radial direction and a weaker orientation with the {011} poles aligned equally in the Z and X-directions. This preferred orientation suggests that this pipe was cast in such a manner that the parameters chosen allowed a few grains to dominate the growth into the liquid melt during solidification after approximately 10 mm from the outside surface of the piping. One the opposite side of the weld joint, the fine equiaxed dendritic microstructure exhibits a texture different than that measured in the columnar region. In the equiaxed region, the dendritic colonies tend to have their <001> poles aligned at a 38° angle to the Y-direction (radial direction), and their <011> planes are aligned with the Y-direction.

Given the variability of the dendritic side, the analysis should be expanded to cover a larger area to ensure that a more accurate determination is made of the texture. The same could be said on the columnar side to see if the {001} preferred orientation is present around the radius of the pipe at different locations. In addition, the change in texture from the upper 10 mm, presumably where the "chill" zone is located, to the larger columnar dendritic structure suggests some changes as a function of depth from the outer surface of the pipe. The current results for the fine dendritic side do not offer enough statistics to confirm if a similar but less optically visual change is beginning to occur.

Future work would benefit from the automated analysis of larger areas of entire sections that could provide a better statistical representation of the texture variation, both at different positions along the radius as well as a function of depth from the outer surface.

A.5 Reference

Porter DA and KE Easterling. 1983. *Phase Transformations in Metals and Alloys*, Van Nostrand Reinhold, p. 234.
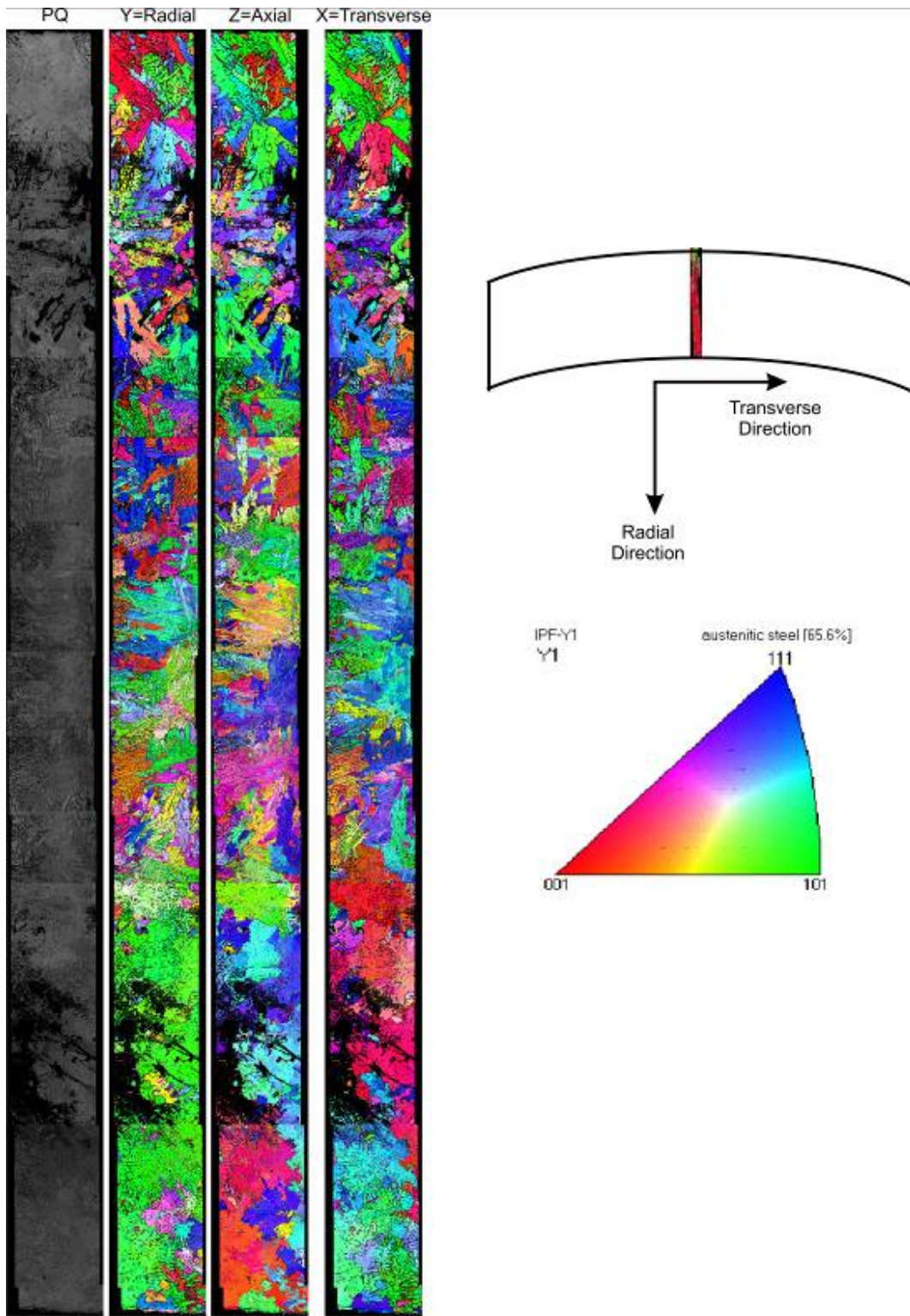
Figure A.7.   A Comparison is Shown of the Pattern Quality Map and the Three Inverse Pole Figure Maps in the y, z and x Directions. Each color maps simply shows the orientation of each region as viewed from the indicated direction. Y is the vertical direction, Z is normal to the page, and X is the horizontal direction.
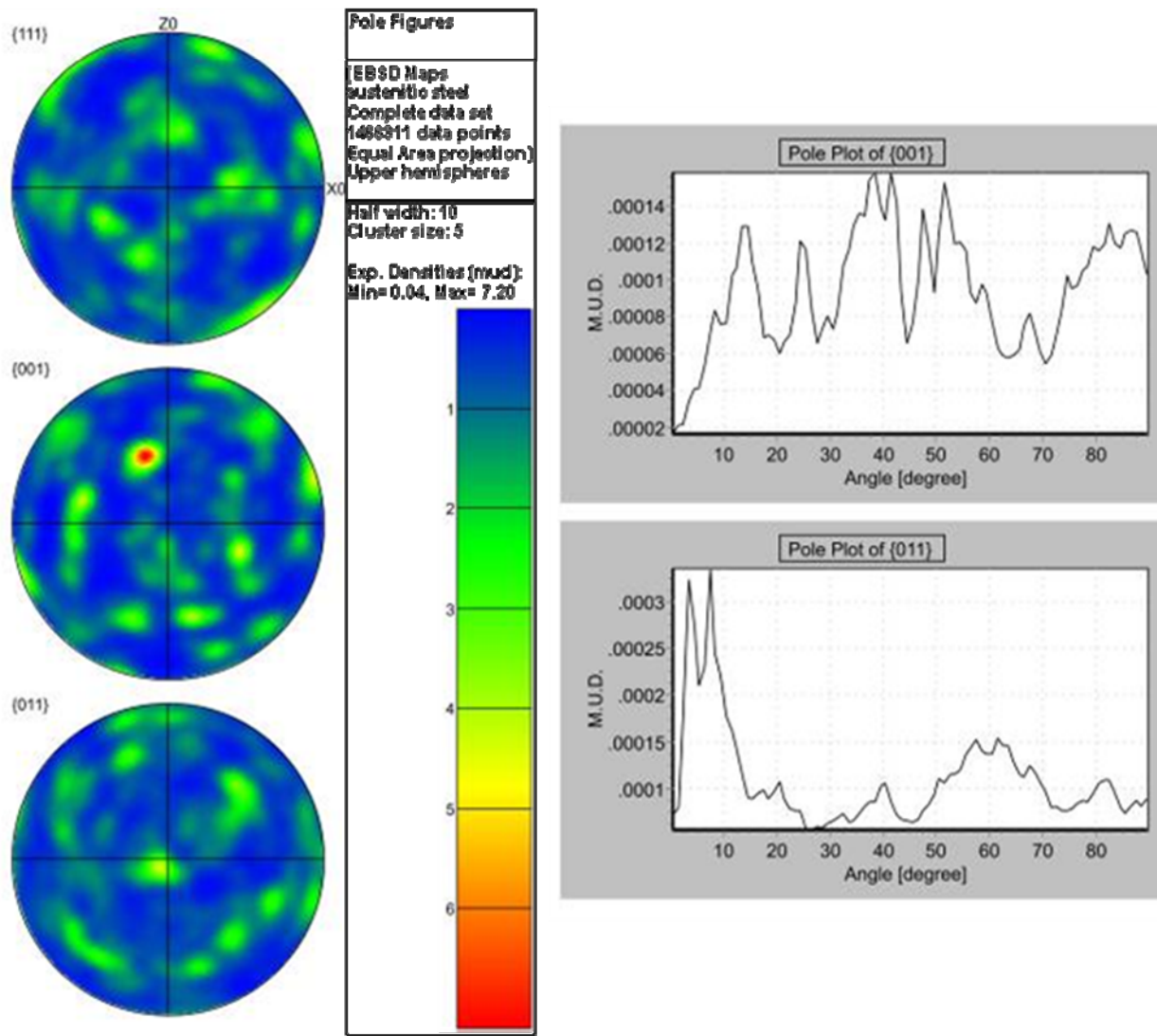
Figure A.8. The Pole Figures Generated from the Entire Orientation Map Across the Fine Dendritic Side Suggest a Moderate Preferred Orientation with the {011} Grains Aligned with the Y-Direction (radial direction) and a Stronger {001} Orientation at a 38° Angle Intermediate between the Radial and Axial Direction. The pole plot histograms show a much different distribution compared to the columnar region, and indicated a strong orientation of the {011} poles aligned to within 10° of the radial direction of the pipe.

Appendix B

Explanation of Electron Backscatter Diffraction Analysis

Appendix B

Explanation of Electron Backscatter Diffraction Analysis

Dan Edwards
Alan Schemer-Kohrn
Clyde Chamberlin

December 2008

The JEOL 840 was operated at 20 keV using a beam current of around 10^{-7} amps. The samples were examined in the SEM in the as-polished condition, that is, no chemical etching was given to the samples. While etching is a common technique for metallography, for SEM work chemical etching introduces topography that can obscure some of the microstructural features of interest, in this case, the grain structure. Etching will in fact reveal the grain structure in many metallic materials, but for this study there were two reasons to use a highly polished and un-etched sample. The first reason is that backscattered electrons are one of the two imaging sources available within the SEM, the other being secondary electrons produced from interactions of the primary electron beam with the sample. While the secondary electron signal reveals topography down to the nanometer level, the grain structure of highly polished metals can be also revealed by virtue of the fact that the high energy elastically backscattered electrons are sensitive to the orientation changes not only between adjacent grains, but also within grain interiors. Backscatter electron images reveal great detail about the grain structure such as grain boundaries, twins, and other structural features. In addition, backscatter electrons are highly sensitive to variations in the average atomic number of the volume of which they interact, so second phases such as oxide particles or precipitates can be easily revealed if the particles are large enough to affect the scattering behavior. As an example, a hundred nanometer diameter particle can be seen in backscatter imaging mode if the average atomic number difference between the particle the surrounding matrix is high enough. Second phase particles of higher average atomic number show up brightly in backscatter electron images because of the higher scattering cross-section, whereas oxides (or to take it to the extreme, porosity and cracks) of the parent material will often show up as a dark region because of the lower average atomic number. All of these features can be obscured to a lesser or greater extent if the sample has sufficient topography to interfere with the backscatter electron signal.

The second reason for using a highly polished sample again relates to the backscatter electrons, but for a different reason. If the sample is tilted to 70°, some fraction of the primary electrons impinging on the sample are backscattered (actually forward scatter would be more appropriate, but in essence they are the same) and produce a Kikuchi diffraction pattern that can be captured using a special detector placed within few 10–25 centimeters of the sample surface. This technique, called electron backscatter diffraction, can be used to obtain crystallographic information about each sample such as grain orientation, types of grain boundaries, grain sizes, and overall texture. Even a small degree of topography distorts the diffraction patterns, so samples for this type of analysis are best examined in a highly polished condition in which all surface deformation is removed. The patterns can be acquired and indexed within ~150 milliseconds, so the technique lends itself to mapping of large areas to create both phase and

orientation maps of the sample surface. In addition, the diffraction patterns can be indexed to reveal the nature of the phase being examined, so when coupled with the compositional measurement capabilities of the SEM, the microstructure can be characterized thoroughly both crystallographically and compositionally at levels down to a few hundred nanometers.

To investigate the grain structure of metallic (or any crystalline material) samples, the SEM electron probe is scanned over finite region chosen to capture the variations in grain structure. At each pixel position, a diffraction pattern is captured and indexed to the appropriate crystal structure. This produces an orientation map of the entire region that shows the individual grains, their crystallographic orientation and the nature and distribution of various interfaces within the mapped region. The EBSD data in this report will be presented in two forms, a pattern quality (PQ) image that reflects a parameter measuring the quality of the individual diffraction patterns and inverse pole figure (IPF) maps. The pattern quality parameter is a function of crystallographic orientation, subsurface deformation, overall strain in the crystal lattice and the acquisition parameters chosen for the pattern acquisition. At this point the PQ is a difficult to define parameter because of the changing contributions from each of the variables that influence the pattern quality, however, it is extremely sensitive and provides a good qualitative understanding of the structure of the material   Even minute scratches not visible in the optical microscope will be revealed because of the degradation in the pattern quality due to the strain in the scratched region.

The inverse pole figure maps are a more complicated form of data to understand. To aid in the understanding of these maps, it helps to understand that in the cubic systems there are three primary crystallographic planes involved in many of the processes of interest, namely solidification and deformation. The three sets of planes, the {001}, {011} and {111} sets, used for inverse pole figures are illustrated in Figure B.1 along with the arrangement of the atoms in the plane of choice. The planes are described by their Miller indices, which are simply the coordinates at which a plane intersects the axis of the cube. In cubic systems, the direction or pole perpendicular to the plane of interest has the same Miller indices, that is, an [001] pole is perpendicular to the (001) plane and so on. In the FCC system, deformation occurs mostly easily along the {111} close packed planes in the [011] direction. Single crystal materials or highly textured polycrystalline materials with a strong {111}/[011] texture in the direction of the deformation axis will therefore behave differently than a material with a random texture. Figure B.1 illustrates how the orientation of a particular grain is assigned a color based on which set of planes is parallel to the polished plane of the sample (in this case the plane of the page). Grains with {001} cubic faces parallel to the polished surface are colored red, grains with {111} planes parallel to the polished surface are colored blue, and grains with the {011} planes parallel to the polished surface are colored green. The bottom drawing in Figure B.2 shows what the grains would look like for a simple case of three grains in the chosen field of view. An inverse pole figure color key is also shown that illustrates the range of colors that can be used. The pole figure actually references the poles perpendicular to the indicated plane, but since there is a 90° relationship between the planes and their respective poles, planes and poles can be used interchangeably. This color key is actually a section of a stereographic projection with shows the angular relationship between the three sets of planes (or their poles). The (011) planes are 45° from the (001) and the (111) planes are 54° from the (001) planes.

It's important to realize that the case in Figure B.2 is highly idealized. For polycrystalline materials such as these electroformed copper samples, the grains will likely exhibit a range of orientations and the orientation maps for the individual grains will therefore be colored according the IPF color key. A full

description of the grain orientation requires two orthogonal map orientations at a minimum to fix the crystal orientation.

A common method for visualizing the degree of texturing, if indeed any is present, is to plot out a pole figure that shows contour lines corresponding to the angular clustering of poles from similarly oriented grains. The pole figure can be chosen to look down any particular axis such as the growth direction of the electroformed copper. The other two directions at 90° to the chosen axis are located on the outer edges of the pole figure circle, thus describing an angular relation between each set of axis in which to plot out the orientation of the grains. Such a pole figure is shown in Figure B.3, and is a color contour plot showing the distribution of poles for the {001}, {011} and {111} planes about the three reference directions R, D, and T. The pole figure reveals some clustering of {111} poles in the center of the pole figure (highlighted by the red circle) and at 90° away near the outer edge of the pole figure in the reference direction (highlighted in orange). Pole figures such as this have to be treated with caution however, since what is really being plotted are the orientations for each pixel position in the image. In other words, unless you have a large number of grains present (>250 grains), an area with a single abnormally large grain could easily skew the pole figure since so many diffraction patterns are present from that one grain.
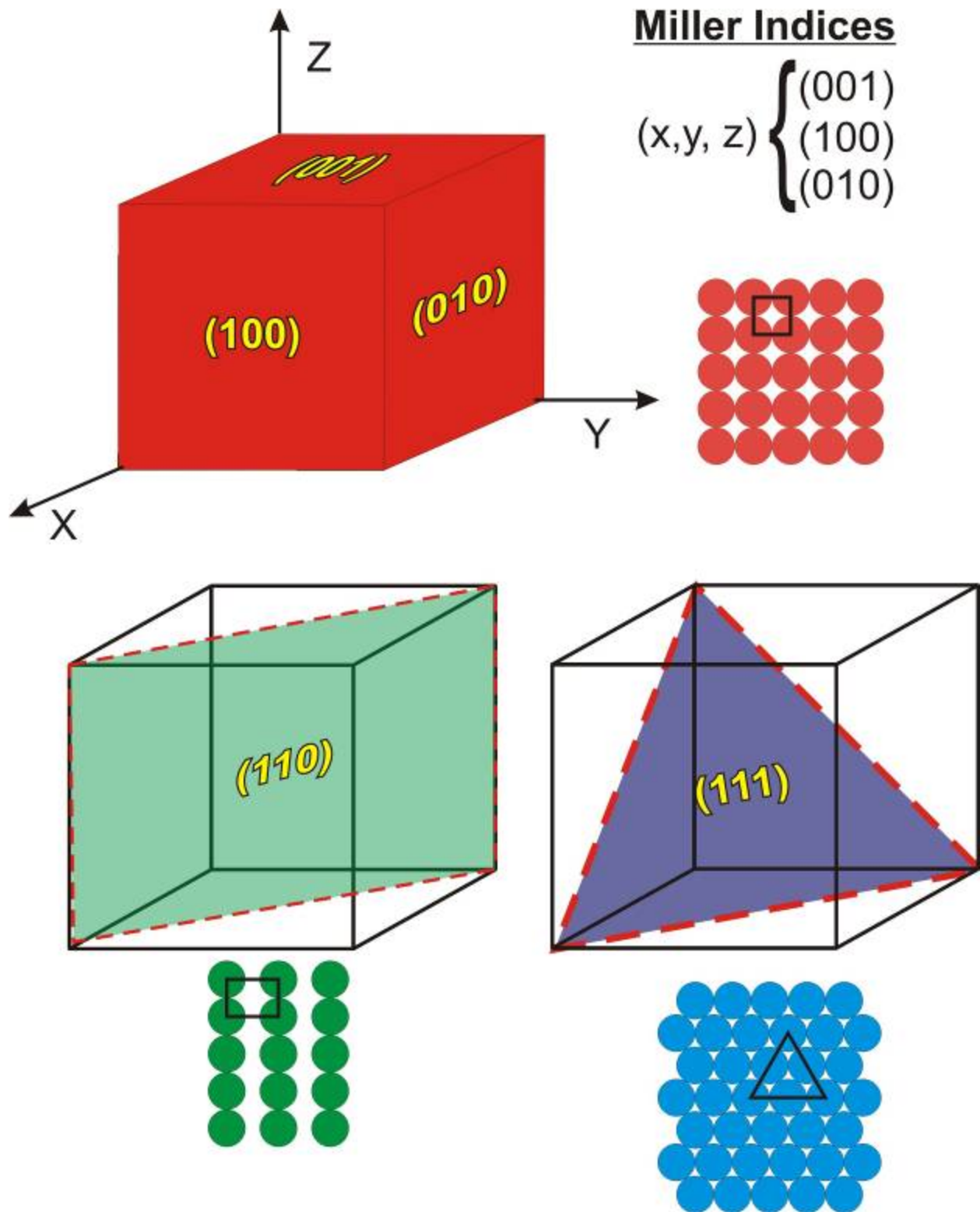
Figure B.1.   Illustration of the Three Primary Crystallographic Planes in the Cubic System, Their Miller Indices, and the Appearance of the Atomic Arrangement on Each Plane
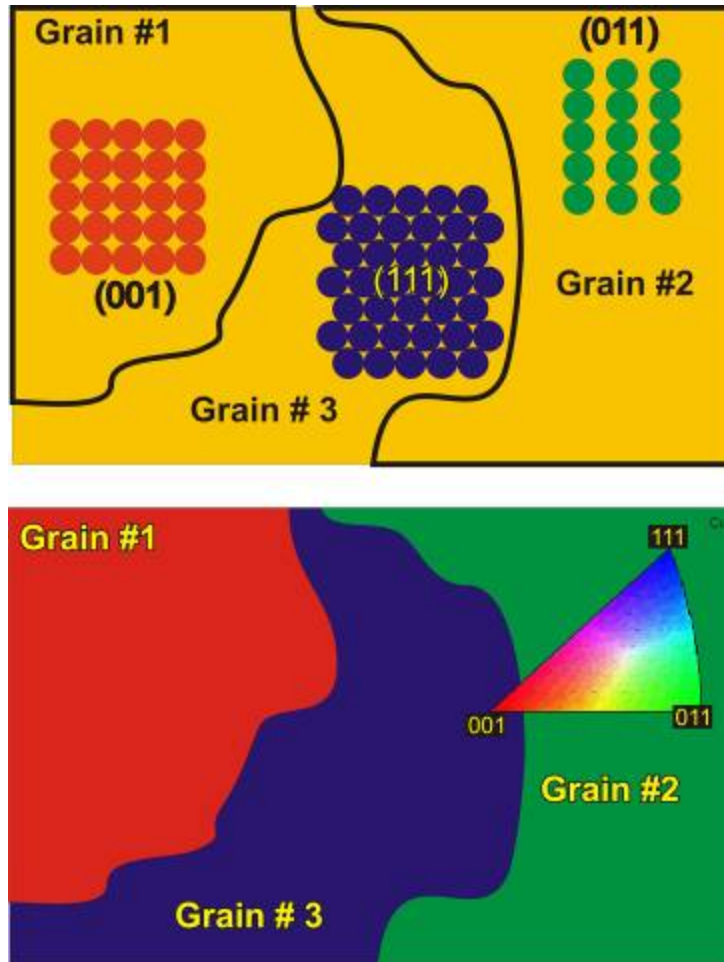
Figure B.2. Illustration of the Color Coding of Individual Grains Based on Their Orientation with Respect to a Particular Axis or Plane
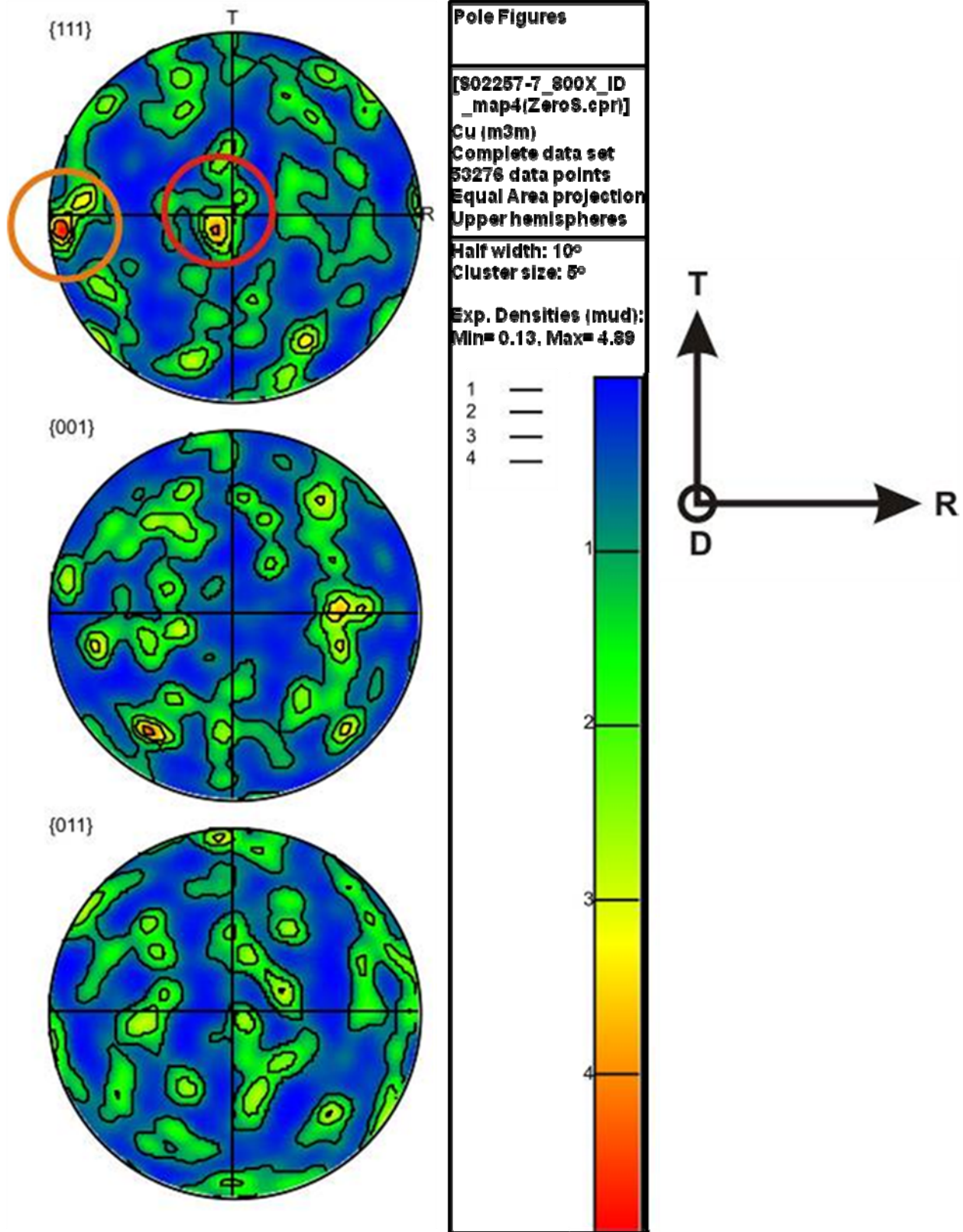
Figure B.3.   Pole Figure Representation of how the Grains are Clustered about Certain Orientations within the Map Shown in the Previous Figure

Appendix C

Calculation of Ultrasonic Attenuation in CASS Specimens – Mathematical Details

Appendix C

Calculation of Ultrasonic Attenuation in CASS Specimens – Mathematical Details

Estimation of the attenuation coefficient for ultrasound may be done using a longitudinal wave pulse-echo technique and utilizing two successive back-wall reflection signals. To derive the attenuation coefficient, we will use a linear systems approach. Let

ω = Angular frequency
D = Specimen thickness
$H_t(\omega)$ = Transfer function of the ultrasonic pulser and diplexer/transducer in transmit-mode
$H_r(\omega)$ = Transfer function of the ultrasonic receiver and diplexer/transducer in receive-mode
$V_i(\omega)$ = Spectrum of applied voltage pulse at the ultrasonic pulser
$V_1(\omega)$ = Spectrum of first back-wall reflection
$V_2(\omega)$ = Spectrum of second back-wall reflection
$H_M(\omega,d)$ = Material transfer function corresponding to ultrasonic path length d.

Then, using linear systems theory (Schmer and Song 2007), we can write

$$V_1(\omega) = H_r(\omega) H_M(\omega, 2D) H_t(\omega) V_i(\omega) \tag{C.1}$$

$$V_2(\omega) = H_r(\omega) H_M(\omega, 4D) H_t(\omega) V_i(\omega) \tag{C.2}$$

The second back-wall signal may be related to the first back-wall signal through the material transfer function and receiver transfer function. The 2D (4D) term in $H_M(\omega,\bullet)$ is due to the use of pulse-echo mode of ultrasonic inspection, which results in a path length corresponding to twice (four times) the specimen thickness for the first (second) back-wall reflection.

For frequencies typically used in ultrasonic NDE, the material transfer function may be approximated as (Schmer and Song 2007)

$$H_M(\omega,d) = \Gamma e^{-jkd} e^{-\alpha d} \hat{D}(\omega,d) \tag{C.3}$$

where Γ is the reflection coefficient, α is the attenuation coefficient and

$$\hat{D}(\omega,d) = 1 - e^{jka^2/d} \left\{ J_0\left(\frac{ka^2}{d}\right) - jJ_1\left(\frac{ka^2}{d}\right) \right\} \tag{C.4}$$

is the diffraction correction term, J_0 and J_1 are the Bessel functions of order 0 and 1, respectively; α is the transducer radius; $k = \frac{2\pi}{\lambda}$ is the wave number; and $j = \sqrt{-1}$.

Thus, from Eqs. (C.1) and (C.2), we have

$$\frac{V_2(\omega)}{V_1(\omega)} = \frac{H(\omega,4D)}{H(\omega,2D)} = \frac{\Gamma_B\Gamma_F\Gamma_B e^{-j4kD}e^{-4\alpha D}\hat{D}(\omega,4D)}{\Gamma_B e^{-j2kD}e^{-2\alpha D}\hat{D}(\omega,2D)}. \tag{C.5}$$

where Γ_B and Γ_F are the (complex) reflection coefficients at the back and front surface of the specimen, for an ultrasonic wave traveling in the specimen. Simplifying Eq. (C.5), we get

$$\frac{V_2(\omega)}{V_1(\omega)} = \Gamma_B\Gamma_F e^{-j2kD}e^{-2\alpha D}\frac{\hat{D}(\omega,4D)}{\hat{D}(\omega,2D)}. \tag{C.6}$$

Define

$$t_A(\omega) = \frac{\hat{V}_2(\omega)}{\hat{V}_1(\omega)} = \frac{e^{j2kD}\left[V_2(\omega)\Big/\hat{D}(\omega,4D)\right]}{\left[V_1(\omega)\Big/\hat{D}(\omega,2D)\right]} = \rho e^{j\theta}e^{-2\alpha D} \tag{C.7}$$

where $\Gamma_B\Gamma_F = \rho e^{j\theta}$. Then,

$$\log_e\left(\left|t_A(\omega)\right|\right) = \log_e(\rho) - 2\alpha D \tag{C.8}$$

or

$$\alpha = \frac{\log_e(\rho) - \log_e\left(\left|t_A(\omega)\right|\right)}{2D} \tag{C.9}$$

The attenuation in Eq. (C.9) is in Nepers per meter, and can be converted to dB/m by using

$$\alpha \text{ in dB/m} = 8.686 \times \alpha \text{ in Np/m} \tag{C.10}$$

Note that the propagation delay correction term in Eq. (C.7) may be written as

$$e^{jk\cdot2D} = e^{j\frac{\omega}{c_p}2D} = e^{j\cdot\omega t_D} \tag{C.11}$$

where $t_D = \dfrac{2D}{c_p}$ is the two-way transit time (or time of flight) for an ultrasonic wave with phase velocity c_p, traveling a distance $2D$. The time-of-flight may be measured easily using the time-domain data. Note further that the resulting compensation for propagation delay is simply a phase correction.

The division operations in Eqs. (C.5) and (C.7), while conceptually simple, cause problems during implementation. The primary issue arises from the presence of zeros (or small values) in the frequency domain representation of the denominator term. Division by these small values causes amplification of any additive noise that is present, resulting in noise terms dominating in the estimation procedure. To mitigate the effect of experimental noise, the division is actually carried out using a deconvolution

(Haykin 1991) procedure. The most common deconvolution procedure is the Wiener deconvolution procedure (Gonzalez and Woods 1999). If

$$\hat{V}_2(\omega) = t_A(\omega)\hat{V}_1(\omega),$$

(C.12)

then the Wiener deconvolution technique determines $t_A(\omega)$ using

$$t_A(\omega) = \hat{V}_2(\omega)\left[\frac{\hat{V}_1^*(\omega)}{\left|\hat{V}_1(\omega)\right|^2 + \dfrac{S_n(\omega)}{\hat{V}_2(\omega)}}\right] = \hat{V}_2(\omega)\left[\frac{\hat{V}_1^*(\omega)\hat{V}_2(\omega)}{\left|\hat{V}_1(\omega)\right|^2 \hat{V}_2(\omega) + S_n(\omega)}\right]$$

(C.13)

where $S_n(\omega)$ is the power spectral density of the noise, the star in the numerator indicates complex conjugation, and the term within the square brackets is referred to as the Wiener filter. If the power spectral density of the noise components is not available (which is the usual case), then we may approximate the expression as

$$t_A(\omega) = \hat{V}_2(\omega)\left[\frac{\hat{V}_1^*(\omega)}{\left|\hat{V}_1(\omega)\right|^2 + \eta}\right]$$

(C.14)

where η is an estimate of the noise-to-signal ratio. The other frequency domain divisions in Eq. (C.7) may also be computed using the same procedure.

Pacific Northwest
NATIONAL LABORATORY

Proudly Operated by **Battelle** *Since 1965*

U.S. DEPARTMENT OF
ENERGY

902 Battelle Boulevard
P.O. Box 999
Richland, WA 99352
1-888-375-PNNL (7665)
www.pnl.gov